Preparation, properties and bioapplications of block copolymers nanopatterns

R. Fontelo[a,b], *R. L. Reis*[a,b], *R. Novoa-Carballal*[a,b,*,#], *I. Pashkuleva*[a,b,*]

[a] 3B's Research Group, I3Bs – Research Institute on Biomaterials, Biodegradables and Biomimetics, University of Minho, Headquarters of the European Institute of Excellence on Tissue Engineering and Regenerative Medicine, AvePark, Parque de Ciência e Tecnologia, 4805-017 Barco, Guimarães, Portugal

[b] ICVS/3B's–PT Government Associate Laboratory, Braga/Guimarães, Portugal

[*] R. Novoa-Carballal e-mail: ramon.novoa@i3bs.uminho.pt; I. Pashkuleva e-mail: pashkuleva@i3bs.uminho.pt

Present address: CINBIO, Universidade de Vigo, Campus Universitario de Vigo, 36310, Vigo, Pontevedra, Spain

Abstract

Block copolymer (BCP) self-assembly has emerged as a feasible method for large-scale fabrication with remarkable precision - features that are not common for most of the nanofabrication techniques. In this review, we present recent advancements in the molecular design of BCP along with state-of-the-art processing methodologies based on microphase separation alone or its combination with different lithography methods. Furthermore, we explore the bioapplications of the generated nanopatterns in the development of protein arrays, cell-selective surfaces, and antibacterial coatings. Finally, we outline the current challenges in the field and discuss the potential breakthroughs that can be achieved by adopting BCP approaches already applied in the fabrication electronic devices.

Key words: self-assembly, protein arrays, nanodevices, cell adhesion, antibacterial surfaces

1. Introduction

Cells are microscopic living entities engaged in continuous communication with their environment. Because of their size, cells actively remodel the extracellular interactome at the micro- and nano- scale and this process plays a critical role in determining their fate.[1] Understanding the bidirectional communication between cells and their environment and the potential application of its principles to guide the cellular behavior has gathered significant interest and research endeavors. Currently, state-of-the-art top-down and bottom-up fabrication methods enable the development of instructive micro- and nano- environments on different substrates without the use of bioactives with limited live time, such as growth factors and adhesion promoters.[1b, 2] For instance, specific nanofeatures such as pits, pillars, groves, or random dots have been identified to enhance the adhesion and differentiation of mammalian cells.[2a, 2b, 2e, 2g, 3] Among different top-down strategies used for the preparation of such instructive topographies, block copolymer (BCP) self-assembly has emerged as a high-resolution, feasible (does not require specific equipment/infrastructure) method that allows large scale fabrication with high fidelity - features that are not common for most of the nanofabrication methods.[4] The diversity of BCP molecular architectures and monomers and the possibility to combine BCP microphase separation with different lithography methods[4-5] make BCP self-assembly a versatile tool for fabrication of medical devices with different applications, e.g. imaging for diagnostics, drug delivery[6], antibacterial coatings, devices that avoid the antimicrobial resistance.[7]

2. Block copolymers: types and fundamentals of microphase separation

Block copolymers (BCP) consist of two or more homopolymers (adjacently polymerized monomers, so-called blocks) that are covalently linked (Figure 1). BCP can be linear, with

sequentially connected blocks (Figure 1A-C) or they can possess complex structures, e.g. star copolymers in which different blocks are linked to the same central point (Figure 1D).

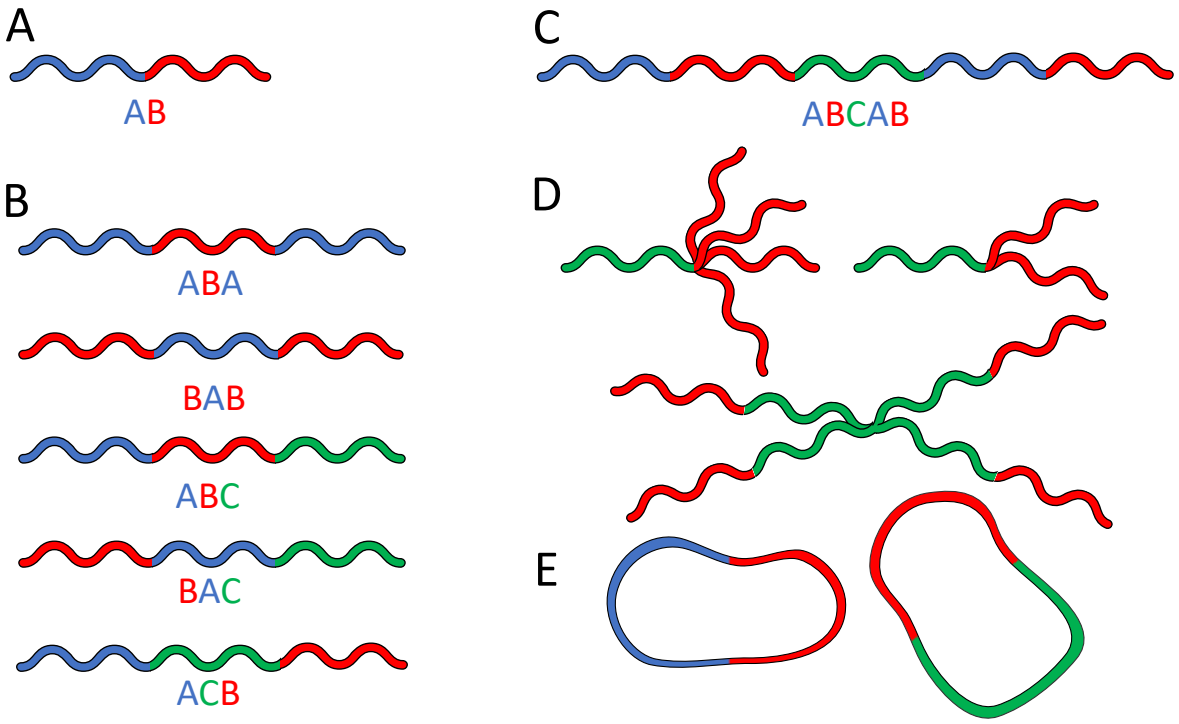

Figure 1. Examples of different types of block copolymers: (A) linear diblock copolymer, (B) linear triblock copolymers, (C) linear multiblock copolymer, (D) star copolymers, and (E) cyclic block copolymers.

When the blocks within BCP are chemically incompatible, a microphase separation occurs - a spontaneous process that results in formation of stable and ordered nanoscopic domains due to intramolecular phase separation in bulk or in concentrated solutions.[8] Fundamental aspects of microphase separation have mainly been studied with structurally simple linear diblock copolymers, although some investigations with triblock copolymers are also reported. As any spontaneous process, the microphase separation is driven by a decrease in the Gibbs free energy ($\Delta G = \Delta H - T\Delta S$). Because the process results in an increased order of the system, i.e. the entropy decreases ($\Delta S < 0$), the temperature and the enthalpy must compensate this reduction

to enable the assembly. Each BCP has a critical temperature above which the self-assembly does not occur. Because in the bulk (i.e., without any solvent), the enthalpy (ΔH) is determined only by the intermolecular forces between the two blocks, the chemistry and the length of the blocks can be tailored to drive the assembly process.

Self-consistent mean-field theory relates the morphology of the generated nanodomains with the BCP properties (Figure 2).[9] In this theory, the morphology of the assemblies is determined by three parameters: the interaction energy between the blocks that is described by the Flory–Huggins interaction parameter (χ) also called segregation parameter; the degree of polymerization, represented by the number of monomers in the BCP (N); and the volume fraction of each block (f).

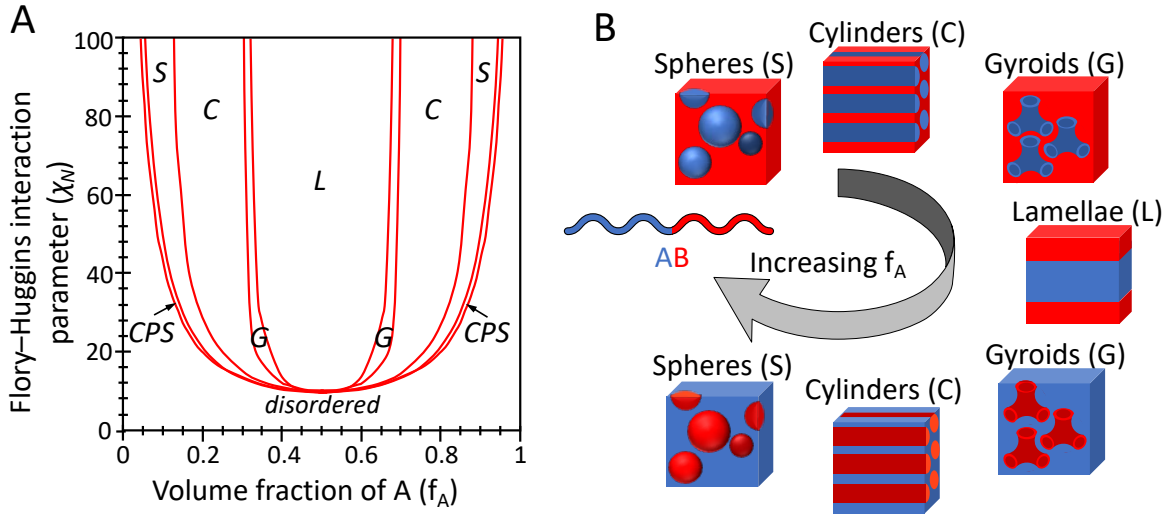

Figure 2. (A) Phase diagram of diblock copolymer obtained using self-consistent mean field theory (S: spheres, C: hexagonally packed cylinders, L: lamellae, G: gyroid, and CPS: closely packed spheres); (B) Illustration of the equilibrium morphologies. Adapted with permission under the terms of the CC BY 3.0 license.[10] 2010, MDPI.

The χ can be determined experimentally and is known for most BCP (Table 1). Microphase separation occurs at relatively low molecular weight for polymers with big χ. Small χ_N ($\chi_N <$ 10) indicate blocks compatibility and homogeneous BCP regardless the f (Figure 2A). On the other hand, $\chi_N > 10$ is associated with increased blocks incompatibility, i.e. blocks segregation, and morphology that varies in function of f (Figure 2B). The phase diagram is useful for initial selection of the size and ratio of the blocks for a targeted application/morphology. In general, the length of the blocks predominantly governs the size of the formed structures, while f determines the morphology of the assemblies (Figure 2B), i.e. spheres, cylinders, or lamellas experimentally observed for diblock copolymers. For example, linear diblock BCP that are composed by blocks with equal size (Fig. 1A, $f_A = f_B$) will assemble into lamellar structure above the order-disorder transition (ODT) (Figure 2A, $\chi_N \approx 10.5$) while BCP for which $f_A \neq f_B$ can form different assemblies. Cyclic BCP have higher glass transition temperatures, lower viscosities, and smaller hydrodynamic volumes when compared to their linear analogues with same composition and degree of polymerization.[11] As a result, their phase diagram is similar to the diagram of the respective linear BCP but the ODT is shifted to a higher segregation strength (χ_N[cyclic] ≈ 1.7 χ_N[linear] and smaller nanostructures.[12] Indeed, experimental data has shown that the spacing between the domains in nanopatterns obtained from cyclic PS-*b*-PEG is decreases by 30% when compared to the patterns obtained from the linear polymer.[11]

Table 1. Common block copolymers for self-assembly of nanopatterns for bioapplications (PS: polystyrene, P2VP: poly(2-vinylpyridine), P4VP: poly(4-vinylpyridine), PEG: poly(ethylene glycol), PMMA: poly(methyl methacrylate), PI: poly(isoprene), PLA: poly(lactide) and their Flory Huggins parameter (data extracted from[13]).

PS-*b*-P2VP $\chi \backsim 0.178$	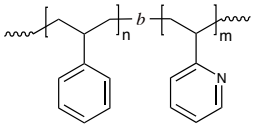	**PS-*b*-PMMA** $\chi \backsim 0.043$	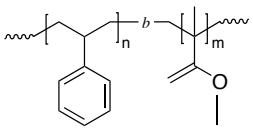
PS-*b*-P4VP $\chi \backsim 0.35$	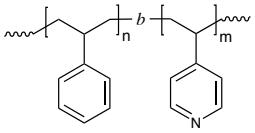	**PS-*b*-PI** $\chi \backsim 0.088$	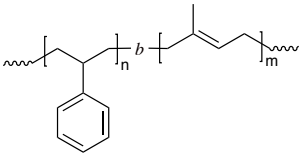
PS-*b*-PEG $\chi \backsim 0.043$	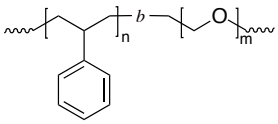	**PS-*b*-PLA** $\chi \backsim 0.217$	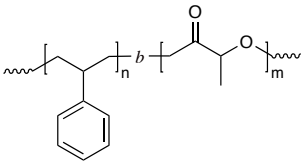

Importantly, this phase diagram (Figure 2) represents the bulk behavior of linear diblock copolymers, considering interactions solely between the blocks without considering the presence of solvents or interfaces. A realistic description of the self-assembly of thin films must consider the BCP interactions with the surface of the substrate onto which the films are deposited as well as the interactions at the air interface. Additionally, the film thickness plays a crucial role in determining the polymer quantity and consequently, the orientation of the domains (parallel or perpendicular to the surface). Theoretical models that integrate these considerations result in more complex diagrams (Figure 3).

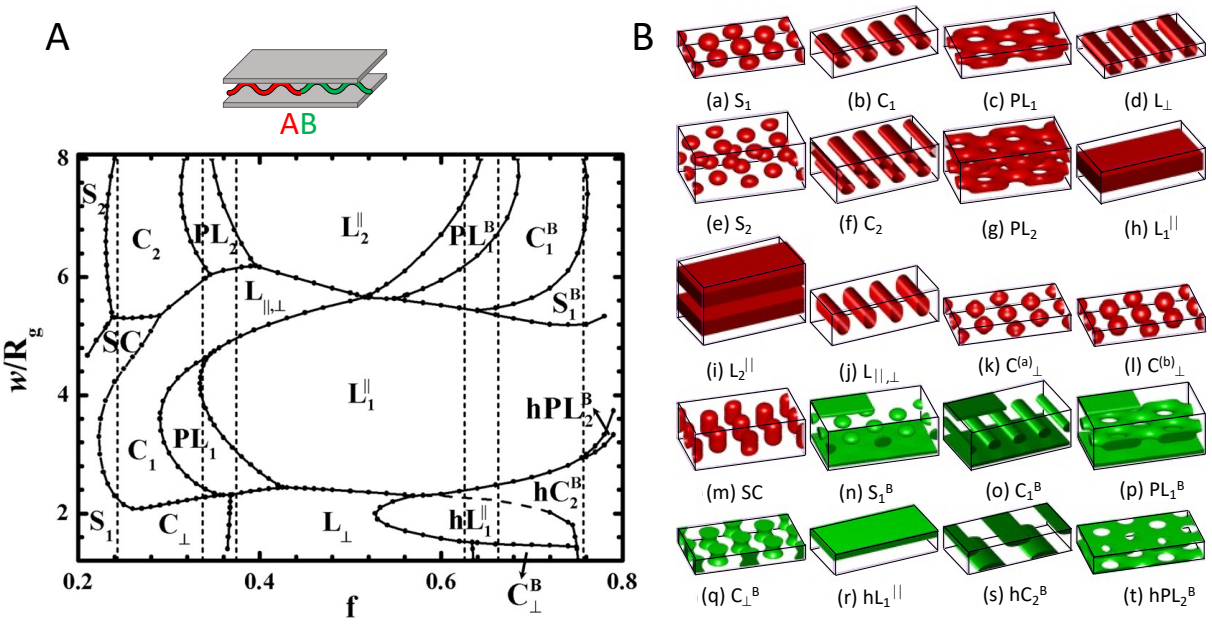

Figure 3. (A) Phase diagram of the self-assembly of a diblock copolymer confined in a thin film between two identical preferential surfaces. (B) 20 morphologies are depicted to construct the two-dimensional phase diagram with respect to the volume fraction and the film thickness, while the interaction parameter χ_N and the surface preferences were fixed. These morphologies are classified into four categories sphere (S), cylinder (C), perforated lamella (PL, corresponding to gyroid phase in bulk), and lamella (L). Adapted with permission from [14]. Copyright 2013 American Chemical Society.

The complexity is amplified when transitioning from di- to tri- and multi- BCP. The use of terpolymers increases substantially the number of possible morphologies (Figure 4): three-color lamellae, cylinders-within-lamellae, knitting pattern, triple and quadruple cylinders-on-cylinders, core-shell cylinders, double and triple helices-on-cylinders, perforated circular layer-on cylinders are some examples of the diverse patterns that can be generated using linear terpolymers.[15] Of note, such diversity is underexplored in the development of bioactive nanopatterns and represents an opportunity for an evolution in this field.

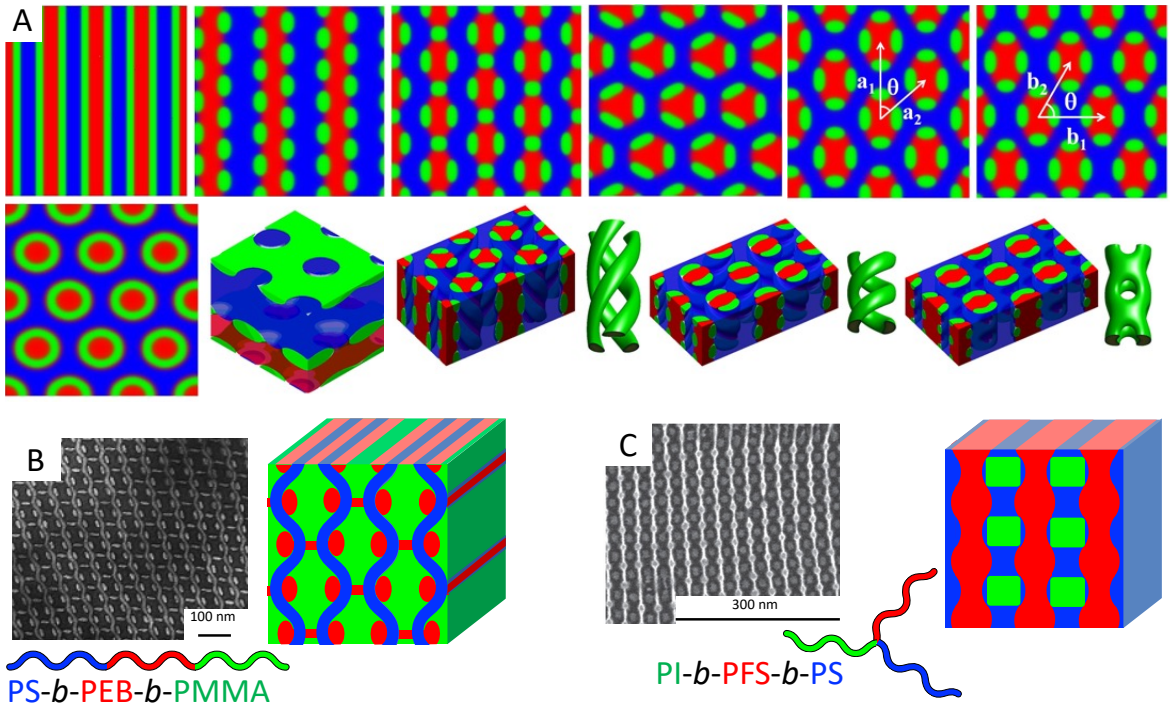

Figure 4. Expanding nanopattern diversity by using triblock copolymers: (A) Density isosurface plots of morphologies formed by ABC linear triblock copolymers (adapted with permission.[15] Copyright 2012, American Chemical Society); (B, C) Experimentally generated complex knitted patterns from (B) linear polystyrene-*b*-poly(ethylene-co-butene)-*b*-poly(methyl methacrylate) (PS-*b*-PEB-*b*-PMMA, adapted with permission.[16] Copyright 2003, John Wiley and Sons) and (C) miktoarm star polymer polyisoprene-*b*-poly(ferrocenylethylmethylsilane)-*b*-polystyrene (PI-*b*-PFS-*b*-PS, adapted with permission.[17] Copyright 2014, John Wiley and Sons) and schematic presentation of the respective microphase separation. The colors show the major component of each region.

While phase diagrams provide insights into microphase separation and aid predicting domain morphology, it is important to acknowledge that certain factors not considered in the models can significantly deviate experimental results from theoretical predictions, as highlighted in various reviews.[13a, 18] As an example, the experimental data for the triblock copolymer

polystyrene-*b*-polybutadiene-*b*-polystyrene (PS-*b*-PB-*b*-PS) showed that the variety of morphologies is limited to cylinders perpendicular to the surface, cylinders parallel to the surface and perforated lamella (Figure 5).[19] Of note is the formation of micro domains with different morphologies instead of an uniform pattern over the whole substrate as a consequence of change in the polymer thickness (Figure 5C). However, this lack of long-range order can be addressed and is further discussed below.

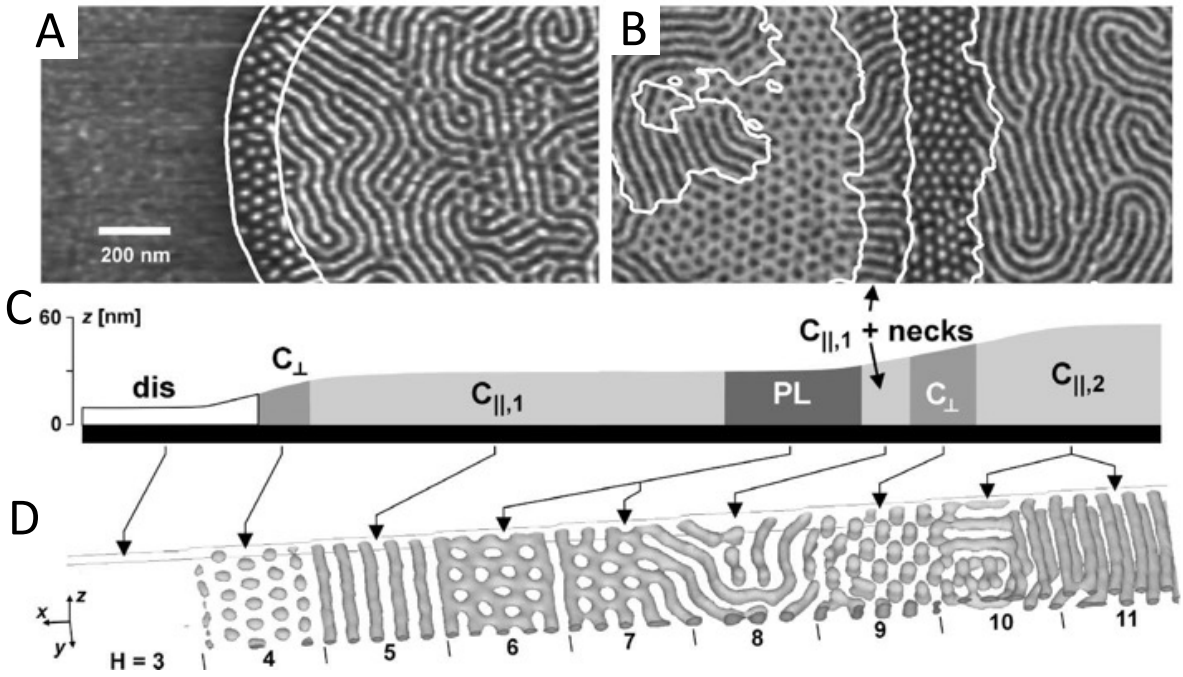

Figure 5. (A, B) Tapping mode AFM images (phase contrast) of polystyrene-*b*-polybutadiene-*b*-polystyrene (PS-*b*-PB-*b*-PS) triblock copolymer after solvent vapour annealing in chloroform. Different domains are delineated with white lines, and correspond to regions of different film thickness. (C) Schematic height profile. (D) Simulated structures of the triblock copolymer. $C_{\perp}$ and $C_{\parallel}$ denote cylinders perpendicular or parallel respectively to the substrate, and PL denotes perforated lamellae. Reprinted with permission.[19] Copyright 2002, American Physical Society.

3. Preparation of block copolymers nanopatterns

The formation of the nanopatterns begins with a deposition of the BCP solution on a substrate, typically performed by spin coating. In this process, several parameters should be optimized to achieve the targeted morphology: (i) the concentration of the polymer solution, which influences the film thickness; (ii) the rotation speed to ensure homogenous spreading of the polymer solution; and (iii) the choice of solvent (whether it is a good or poor solvent for the blocks and its evaporation rate).[7a, 7b, 20] Dip-coating has been used as an alternative to spin coating[21] but our experience showed that this method tends to be less reproducible and controllable.

The deposited BCP film often lacks long-range ordering due to the uncontrolled evaporation of the solvent and the resulting nonequilibrium effects.[22] Such order can be induced by an additional step called annealing - a process of blocks re-ordering towards an equilibrium state. Thermal and solvent vapor annealing are the most common methods but more options exist, such as photothermal annealing,[23] electric or magnetic induced annealing,[24] annealing by solvent immersion,[25] and combinations of different annealing methods that enable the formation of more complex structures.[26]

3.1. Thermal annealing

Thermal annealing aims to increase the mobility of the blocks and consists in heating the BCP thin film above the glass transition temperature (T_g) but below the ODT temperature. This process is typically carried out under vacuum or in the presence of inert gas and can last from few hours to days.[22] Annealing in air, at atmospheric pressure can be also performed using rapid heating methods such as microwave heating[27], photothermal laser heating[28], and infrared radiation[29] - methods that can reduce the annealing time to minutes. The specific

annealing parameters such as temperature and duration depend on the BCP characteristics, namely molecular weight, f, χ and the film thickness.[4, 30] As the χ value increases, the diffusion coefficient decreases, which is translated into prolongation of the annealing periods to accomplish effective microphase separation. The thermal annealing is not feasible for BCP with high molecular weights or high χ, because of the required very high temperatures (ODT temperature > degradation or chain scission temperature) or prolonged annealing times that can destroy the polymer.[31] For these BCP, solvent vapor annealing is used instead.

3.2. Solvent vapor annealing

When the T_g of BCP is lowered below room temperature by using a solvent vapor, the process is referred to as solvent vapor annealing (SVA). In SVA, the solvent molecules interact with/swell the BCP film, thus, reducing the diffusive energy barrier and enabling microphase separation at low temperatures. The BCP film is placed in a closed system with a saturated atmosphere of solvent or mixture of solvents. SVA has several advantages over thermal annealing. A major advantage is the significant reduction of the time required to reach an equilibrium state: whereas thermal annealing can take hours to days, SVA can result within hours to minutes.[32] Additionally, SVA provides the opportunity to fine-tune the morphology by choosing solvent(s) that selectively swells one block, effectively changing the volume fraction and driving morphological changes[33], e.g. we have demonstrated that micelles formed during the spin coating of polystyrene-*block*-poly(2-vinyl pyridine) (PS-*b*-P2VP) in toluene can be transformed to lamellae after SVA in chloroform[7a, 7b, 34]. The domain size and spacing can be tailored with the solvent pressure, while the solvent removal rate affect orientation and correlation length of microdomains.[26, 31a] However, a main drawback of SVA is the lack of standardized annealing apparatus, which turns the reproducibility and comparison of the BCP patterns generated by SVA challenging.[8a, 35] As an example, the introduction and the removal

of the solvent vapor into the annealing chamber can be different. Most common setups use a vessel with the solvent placed inside a sealed chamber together with the BCP sample.[7a] In this configuration, there are several variables that can affect the generated pattern: the amount of the solvent; the vessel shape and volume that affect the evaporation rate of the solvent; the chamber volume, humidity, and temperature that affect the vapor pressure. A superior control is provided by an alternative setup, in which the annealing chamber is equipped with a controlled flow of inert gas that allows adjustable vapor pressures.[31a] However, control over the rate of the solvent removal is challenging in both configurations. To address this shortcoming, a SVA setup with an inert gas that passes via the vessel with the solvent and carries the vapors to the annealing chamber has been used.[31b] The inert carrier gas allows for control of the vapor pressure inside the chamber and controlled solvent removal (by controlled purging). Of note, very high solvent vapor pressure is not achievable in this setup because the inert carrier gas dilutes the solvent vapor.

3.3. Template-driven long-range ordering

An alternative approach to induce long-range order is to cast the BCP film on micropatterns obtained by lithography or chemical etching, among others (Figure 6A). The spatial confinement of the BCP in the micropattern trenches induces nucleation, i.e. ordering of self-assembled nanodomains along the template edge. The spontaneous close packing of neighboring nanodomains raises the order propagation from the confining walls of the template that ultimately leads to reorganization/alignment of the microdomains.[36] This process, known as graphoepitaxy, enables the creation of a hierarchical organization with two length scales on a single substrate. The surface chemistry of the template, the thickness of the casted BCP, and the size of the blocks are crucial for the nucleation of the microdomains and can be tailored to

induce different organization at the nanoscale within the same micropattern (Figure 6B, C).[36a, 37]

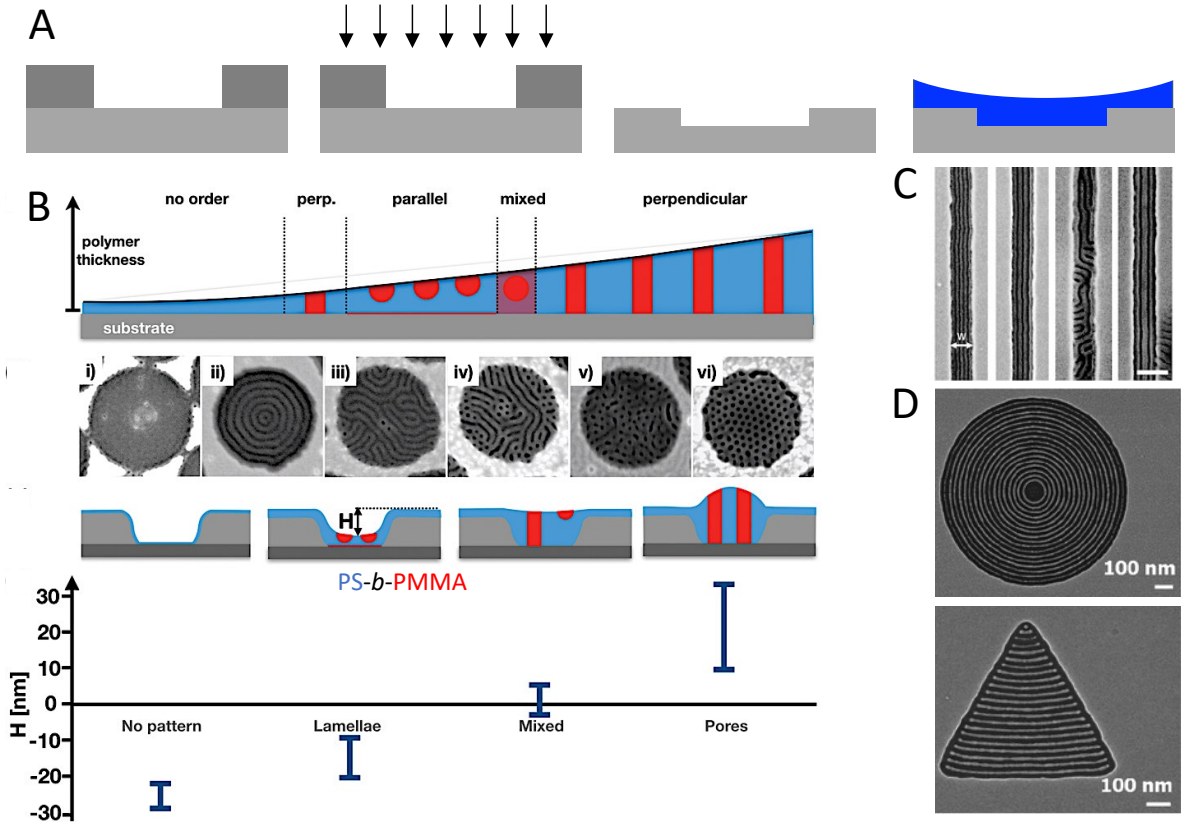

Figure 6. (A) Schematic presentation of the experimental steps in the development of template-driven long-range ordered BCP nanopatterning. (B) Effect of the thickness on the morphology of the nanopattern assembled from PS-*b*-PMMA assembled on nanopore template. Reprinted with permission under the terms of the CC BY 4.0 license.[37b] 2019, John Wiley and Sons. (C) Effect of molecular weight of PS-*b*-PMMA (from left to right 36, 66, 74, 104 kDa) on the domains' morphology of patterns assembled on template modified with hydroxyl-terminated random copolymer PS-*r*-PMMA (styrene fraction 0.47). Scale bar 200 nm. Reprinted with permission.[36a] Copyright 2010, John Wiley and Sons. (D) Examples of long range ordered nanopatterns obtained by casting of PS-*b*-P2VP films on micropatterns on silicon obtained by e-beam lithography. Adapted with permission.[38] Copyright 2008, American Chemical Society.

Recent works have explored more complex templates such as hemisphere[39] and asymmetric hemisphere nanocavities,[40] at which different confinement of the casted BCP drives formation of patterns with customized size and morphology. These works have shown the potential of the template-driven assembly of BCP for generating great diversity of complex and defect-free morphologies: straight lines, concentric circles, spirals, square arrays of dots, bends, T-junctions are just few examples of the versatility of this method (Figure 6D).[18, 36b, 37a, 39-40] However, the widespread implementation of this method is hindered by the specific and often costly equipment needed for the preparation of the substrates. So far, it is mainly employed in the fabrication electronic devices and its use in the context of biological applications remains limited, despite the immense possibilities that it offers. 3D templates are also underexplored mainly due to challenges associated with homogeneous deposition of BCP on such templates and thus, problems with long-range ordering. However, the use of BCP with rod-coil conformation (Figure 7A) allows formation of nanopatterns by simple immersion of the substrate without following annealing.[41] The feasibility of this approach has been demonstrated for substrates as carbon nanotubes (Figure 7B)[42]and microspheres (Figure 7C)[43] and has great potential for further development of biofunctional materials and biosensors.

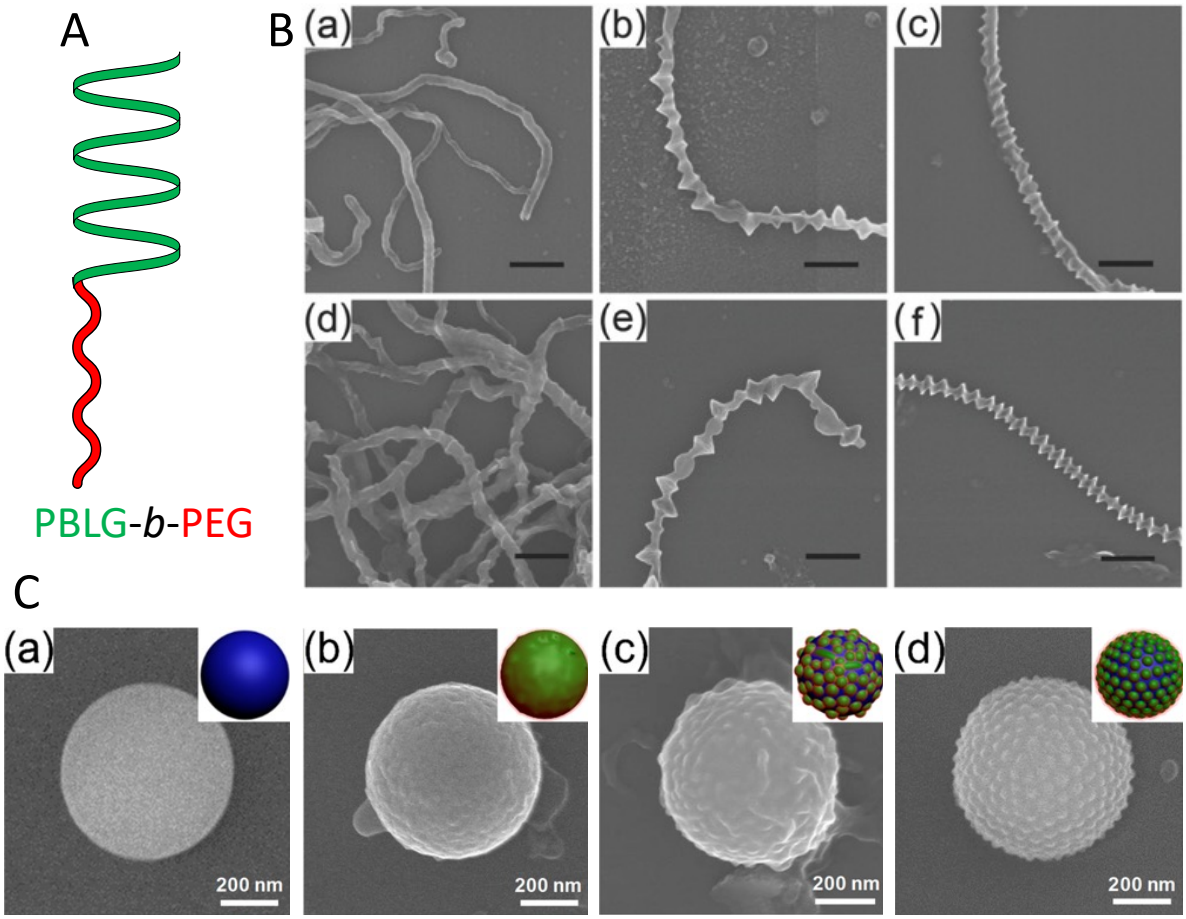

Figure 7. (A) The rod-coil conformation of poly(γ-benzyl-l-glutamate)-*b*-polyethyleneglycol (PBLG-b-PEG) allows assembly of nanopatterns on 3D structures. (B) Effect of the solvent and temperature on the PBLG-b-PEG assembly on carbon nanotubes: a) DMF, 30 °C; b) dioxane, 30 °C; c) DMF/dioxane (1/1 in volume), 30 °C; d) DMF, 60 °C; e) dioxane, 60 °C; and f) DMF/dioxane (1/1 in volume), 60 °C. Adapted with permission.[42] Copyright 2018, John Wiley and Sons. (C) Morphology evolution of the surface nanostructures with the addition of water to the initial solvent (THF/DMF, 3/7 v/v): (a) 0, (b) 13.0, and (c) 28.6 vol % of water contents, (d) After dialysis against water. Adapted with permission.[43] Copyright 2019. American Chemical Society.

4. Bioapplications of BCP nanopatterns

4.1. BCP nanopatterns as templates for proteins adsorption

While protein-based BCP are widely used for bulk assembly of 3D bioactive nanostructures, most of the BCP used for nanopatterns development are biologically inert. This choice has been imposed by the processing conditions (e.g. temperature annealing, annealing in organic solvents) that are incompatible with sensitive protein/peptide blocks. However, there are few recent studies that use the peptide-based poly(γ-benzyl-l-glutamate)-*b*-PEG (PBLG-*b*-PEG) to assemble nanopatterns but their biofunctionality is not demonstrated.[41-44] To overcome this limitation, protein nanoarrays can be obtained by using BCP nanopatterns as templates (Table 2). There are different approaches that can be used for protein immobilization/order and the choice depends on the structure of the protein and the intendent application.

Table 2. BCP nanopatterns used in development of protein arrays. BSA: bovine serum albumin, IgG: immunoglobulin G; HRP: horseradish peroxidase, MT: mushroom tyrosinase, GFP: green fluorescence protein, HEMA: poly(2-hydroxyethyl methacrylate).

Block copolymer	**Annealing**	**Protein**	**Protein ordering method**	**Ref**
PS-*b*-PB	Thermal	BSA, fibrinogen, cytochrome C, IgG	Electrostatic interaction	[45]
PS-*b*-PEG	SVA	PEGylated Lsmα	Co-dissolved with BCP	[46]
		PEGylated lysozyme	Co-dissolved with BCP	[47]

PS-*b*-P4VP	SVA	Anti-IgG	Selective adsorption to hydrophobic domains	[48]
PS-*b*-P4VP	None	IgG, HRP and MT		[49]
PS-*b*-PMMA	Thermal	HRP		[50]
		GFP		[50a]
		FITC-anti IgG		[50a]
		Fibronectin		[50b]
		FITC-IgG		[51]
		Fibrinogen		[52]
		IgG		[50a, 50b, 51, 52b, 53]
		BSA		[50a, 50b, 52c, 53]
		MT		[50a]
		Protein G		[50a, 50b, 51]
PS-*b*-PI	Thermal	BSA		[54]
PS-*b*-PHEMA	SVA	His-GFP	DA/Cu^{2+}/poly-His chemistry	[55]
PS-*b*-PHEMA	SVA	Fibrinogen, myoglobin and lysozyme	Click chemistry	[56]

The simplest approach consists in an incubation of the protein with a BCP nanopattern that trigger selective protein adsorption on the microdomains assembled from one of the blocks.[49-50, 50c, 51] For example, IgG adsorbs exclusively on the PS cylindrical domains generated by microphase separation of PS-*b*-PMMA (Figure 8).[50b, 50c] Interestingly, IgG adsorbs on homogeneous PMMA substrates but not on the PMMA areas in the BCP pattern.[50b] Moreover, the amount of the IgG adsorbed on the BCP pattern is higher than the protein adsorbed on PS/PMMA blends or plain PS surfaces. Another interesting observation is that on PS/PMMA blends, the protein adsorbs preferentially on the PS area that is close to the PMMA interphase (Figure 8). This preference can be explained by the amphiphilic character of proteins (with hydrophobic and hydrophilic regions).[57]

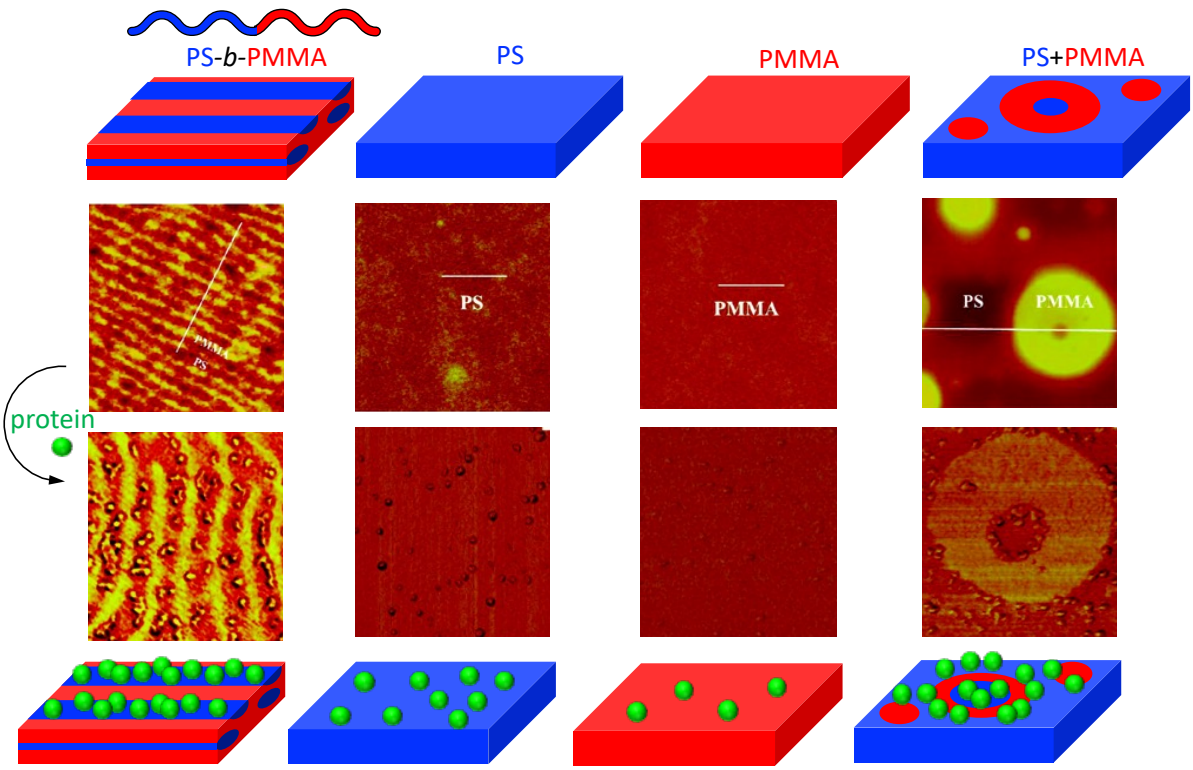

Figure 8. Protein (IgG) adsorption on nanopatterns assembled from PS-*b*-PMMA and the respective controls: substrates from PS, PMMA, and blend of PS and PMMA. Adapted with permission.[50b] Copyright 2008, American Chemical Society.

The shape and size of the proteins that interact with BCP nanopatterns are also important. Lau *et al* defined empirically the relation between the protein size and domains size for PS-*b*-PMMA nanopatterns: using BSA (66 kDa; 8x7x4 nm^3) and IgG (150 kDa; 14x9x4 nm^3) as protein models, they observed a higher adsorption affinity on PS domains whose size is 3-folds less the size of the protein.[53] Fibrinogen (Fg) is larger (340-420 kDa) and has a higher aspect ratio (47x5 nm^2) than BSA and IgG. Its adsorption on the PS-*b*-PMMA nanopatterns is illustrative example of the interplay between nanodomain size and protein size. Upon adsorption, Fg can adopt three different conformations, which depend on the size of the polymer domains and the protein concentration (Figure 9).

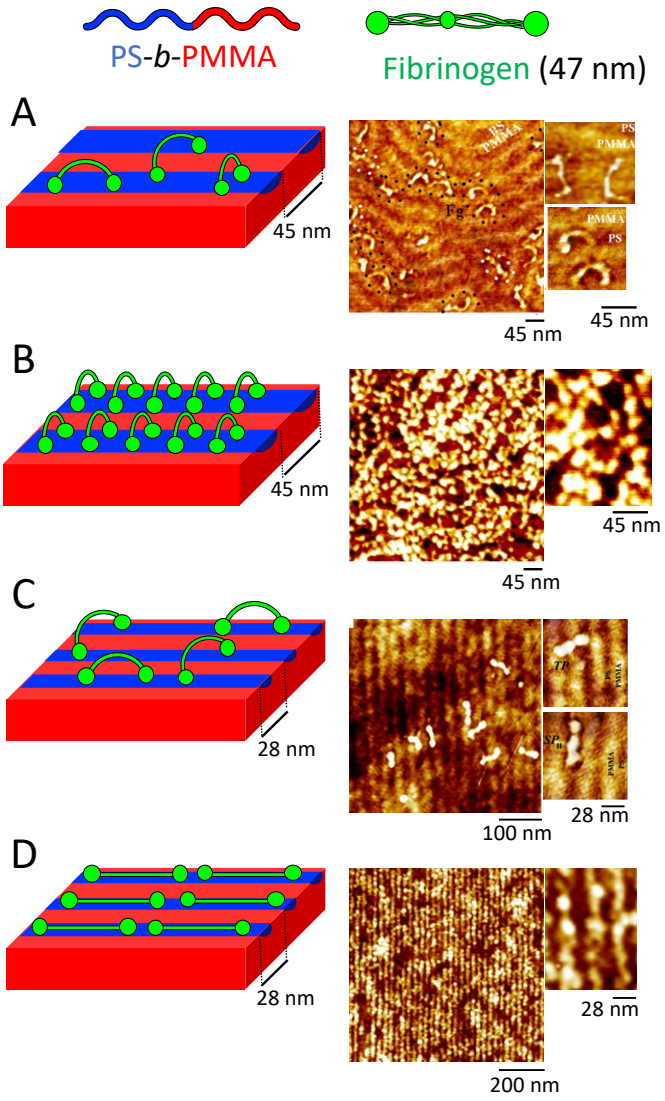

Figure 9. Schematics presentation and AFM images showing fibrinogen adsorption on PS-*b*-PMMA nanopatterns with periodicity of 45 nm (A, B) and 28 nm (C, D). Different protein concentration (2.5 and 20 μg/mL) was used and the AFM images show data for low (A, C) and high (B, D) protein coverage. Adapted with permission.[57] Copyright 2021, American Chemical Society.

The manipulation of the protein conformation by the underlying pattern is of interest especially in the case of enzymes: the bioactivity of the immobilized enzymes relies on the exposition of their active center after adsorption. Several studies have demonstrated that enzymes adsorbed on the PS domains retain their catalytic activity for months.[49-50, 50c] However, few enzymes have been studied to date, and the data cannot be generalized. Specific molecular dynamic simulation studies are emerging to address this topic.[57]

Besides PS-*b*-PMMA, other BCP such as PS-*b*-PVP[49], PS-*b*-poly(2-hydroxyethyl methacrylate) (PS-*b*-PHEMA)[58] and PS-*b*-polyisoprene (PS-*b*-PI)[54, 59] have been used to develop nanopatterned substrates for protein immobilization. Most of the studies have focused on single protein solutions and little is known about competitive and/or cooperative interactions with protein mixtures. One of the major challenges in such studies is the differentiation of the proteins adsorbed on the pattern. The main analytical tool used for characterization of such systems is AFM as it offers high resolution and ability to work in wet environment but it does not provide composition information. To date, only a few two-component mixtures containing proteins that can be identified by AFM (e.g. IgG and Fg; BSA and Fg) have been explored and only on PS-*b*-PMMA nanopatterns.[52b, 52c] The results showed that the smaller protein adsorbs faster on the patterns but is subsequently displaced by the larger protein, demonstrating the validity of the Vroman effect for BCP nanopatterns. However, this effect is delayed when compared to proteins adsorption on homogenous PS surfaces due to the stronger protein

attachment (i.e., lower mobility) at the domains interface, involving both hydrophobic and hydrophilic binding moieties of the protein.

The difference in protein size and chemical affinity to the blocks can be effectively used to develop patterns of two proteins. An illustrative example is the consecutive deposition of IgG and BSA on PS-*b*-PMMA nanopatterns: IgG, which has a high affinity to PS, is adsorbed first, followed by BSA adsorption on the PMMA domains.[53] Chemical functionalization of one (or more) of the blocks can be used to enhance the protein affinity with the domains assembled by this block. Functionalization with charged[45] or hydrophilic[58] groups is a straightforward approach but the domains assembled from the modified blocks can swell in buffer media hindering the expected effect.[45, 58] Biotinylation is another alternative: the formed biotinylated domains are functionalized with the complementary avidin and in the next step biotinylated molecules are deposited to create the pattern (Figure 10A).[60] When the other block bears photocrosslinkable functional group (Figure 10B), hierarchical patterns can be developed using BCP self-assembly to generate the nanopattern and a photomask to create the micro pattern (Figure 10C, D).

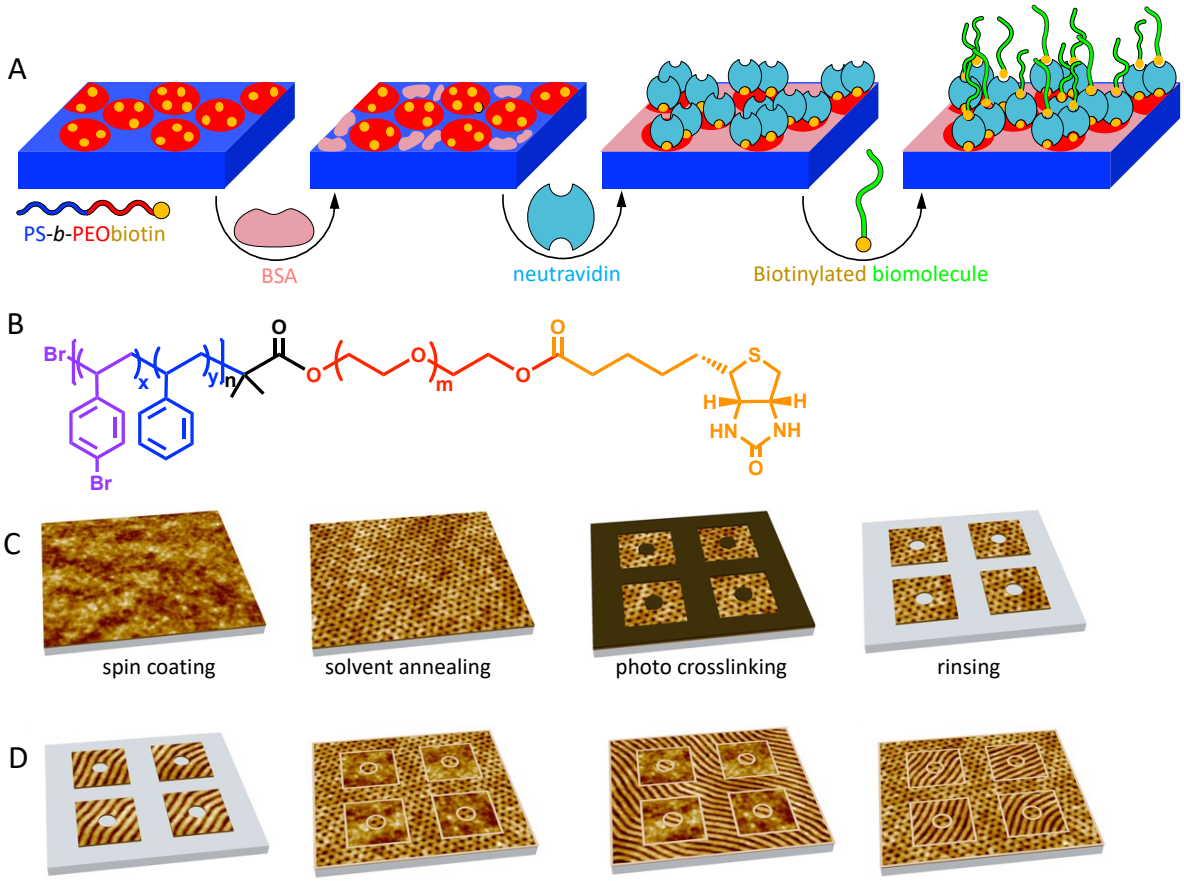

Figure 10. (A) Schematic presentation of different steps in the preparation of protein nanopatterns using biotinylated BCP. (B) PS-*b*-PEO polymer functionalized with crosslinkable group (purple) at the PS block (blue) and biotinylated (orange) PEO block (red). (C) Consecutive steps in the preparation of hierarchical patterns from the modified PS-*b*-PEO and (D) examples of different patterns generated by this approach. Adapted with permission.[60] Copyright 2014, American Chemical Society.

Instead of chemical modification of the blocks, the BCP domains can be functionalized by addition of a polymer that is mixable only with one of the blocks. For instance, a mixture of PS-*b*-PHEMA and PS end-functionalized with iminodiacetic acid groups (IDA) results in assembly of nanopatterns where the PS domains bear IDA and can be used for further immobilization of histidine-tagged protein (Figure 11).[55]

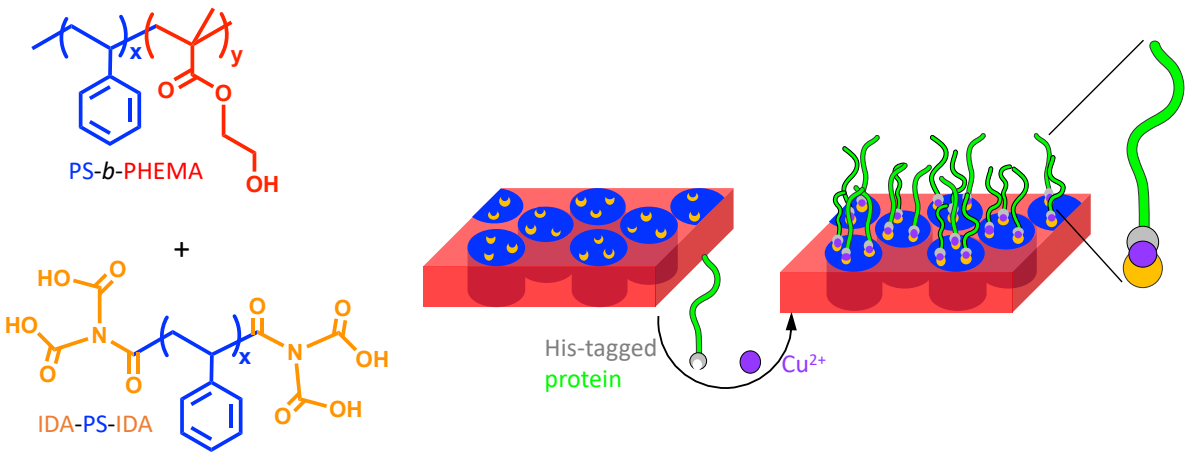

Figure 11. Schematic presentation of the preparation of protein nanopatterns by mixing structural block copolymer PS-*b*-PHEMA and a functional polymer IDA-PS-IDA to generate domains with high affinity for his-tagged proteins. Adapted with permission.[55] Copyright 2016, John Wiley and Sons.

In a different strategy, Spatz *et al* have proposed to use BCP nanopatterns as a sacrificing template for printing peptides.[61] The advantage of this approach is that the space between individual peptides can be precisely controlled. The method uses PS-*b*-P2VP because of the P2VP ability to complex with metal salts (Au, Pd, or Pt). PS-*b*-P2VP is dissolved in toluene to form micelles with PS shell and core of metal doped P2VP. A film is casted and treated by plasma to remove the polymer and expose the metal nanoparticles that are then used as anchors for end-on thiol/cysteine peptide (Figure 12A). The spacing between the nanoparticles can be tuned by the molecular weight of PS and P2VP blocks (Figure 12B).[5c, 61-62] This spacing is important for cell attachment and spreading - decreased cell spreading and a reduced adhesion force was observed for fibroblast, osteoblast, and melanocytes when the spacing between the RGD-functionalized nanoparticles exceeds 58 nm (Figure 12B). This behavior is related with an impaired integrin clustering at larger spacing and suggests a universal length scale for integrin clustering and activation given the similar response of different cells.

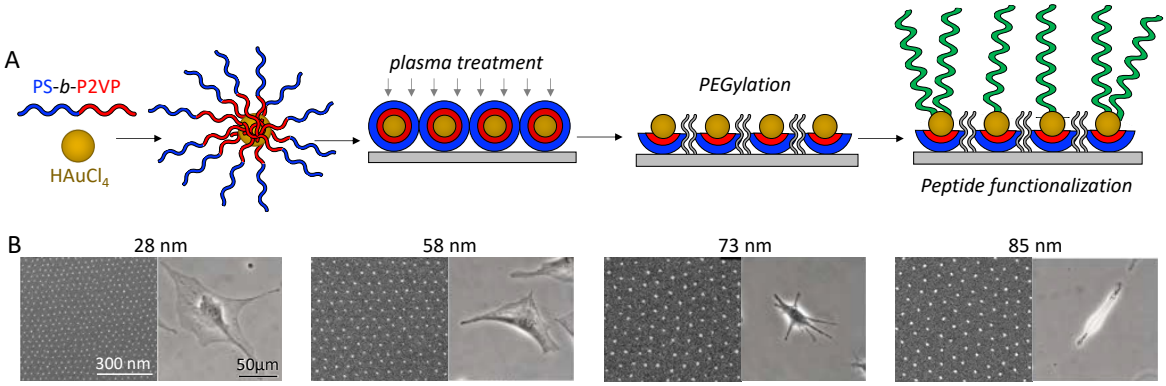

Figure 12. (A) Schematic presentation of the main steps for the development of peptide nanoarrays by using BCP sacrificial templates. (B) Examples of RGD nanoarrays with different spacing and their effect on cell spreading, adapted with permission.[61] Copyright 2016, John Wiley and Sons.

The approach can be extended to proteins. For instance, a nanoarray featuring the transmembrane protein DM-GRASP was used to investigate the role of this protein in neuron attachment and neurite outgrowth.[63] Neurons were studied on nanoarrays with different spacing (29 - 137 nm) and the results showed that neurite formation was increased at higher DM-GRASP density except for the array of 70 nm. These data allowed to identify the spectrin binding sites for DM-GRASP.[63]

4.2. Control of cell adhesion and differentiation by BCP nanopatterns

The ability to control the protein adsorption on BCP nanopatterns demonstrates the possibility to use these patterns to manipulate cell behavior (Table 3).

Table 3. Examples of BCP nanopatterns modified by peptides/proteins and used for cells culture. SVA: solvent vapor annealing; N.A. not applied; BSA: bovine serum albumin, FBS: fetal bovine serum; hMSC: human mesenchymal stem cells; ADA: adamantin.

Block copolymer	**Annealing**	**Protein/peptide**	**Protein immobilization method**	**Cells**	**Ref**
PS-*b*-PEG	SVA	BSA, FBS, Fibronectin, Collagen	Selective adsorption	Murine chondrocytes	[64]
PS-*b*-PEG	N.A.	Fibronectin, RGD, laminin, IKVAV, YIGSR, RRETAWA, a5b1	Maleimide	NIH-3T3 hMSC	[65]
PS-*b*-PEG	N.A.	RGD, IKVAV, E-cadherin, N-cadherin, heparin, decorin, Collagen	ADA + β-cyclodextrin	hMSC	[66]
PS-*b*-PEG	N.A.	RGD and IKVAV	N_3 and ONH_2 terminals on PEO.	hMSC	[67]
PS-*b*-PEG	SVA	IgG	Biotinylation	hMSC	[60]

PS-*b*-PI	N.A.	Fibronectin	Deposition	Chinese Hamster Ovary (CHO)	[59]
PS-*b*-PMMA	Thermal	Fibrinogen	Deposition	C57/Bl6 mice microglia	[68]

An early study by Hutmacher *et al* showed that indeed cells can sense and respond to nanotopographical cues.[69] In their study, dermal fibroblasts and mesenchymal precursor cells were cultured on micellar nanopatterns obtained from PS-*b*-PV2P and lamellar PS-*b*-PV4P patterns (Figure 13). Interestingly, a higher number of adhered cells were observed on the lamellar nanopatterns, irrespective of the cell phenotype. This result can be explained with the compact protein packing facilitated by the lamellar pattern. These findings underscore the influence of nanotopography on cell behavior, highlighting the significance of surface features in cell adhesion and response.

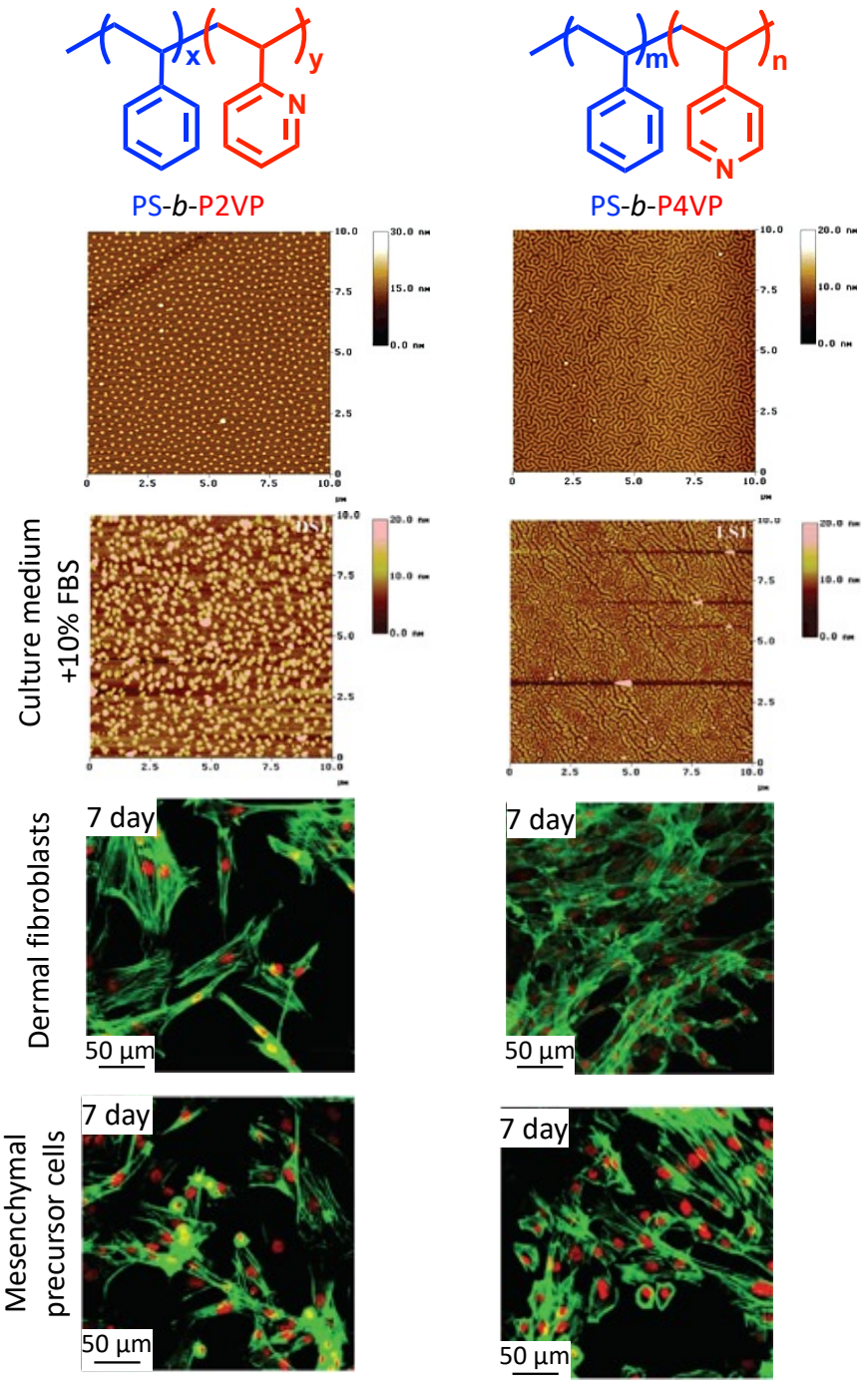

Figure 13. Effect of BCP nanopattern morphology on the adhesion and spreading of dermal fibroblast and mesenchymal precursor cells. Adapted with permission.[69] Copyright 2007, American Chemical Society.

Following this study, we performed a systematic investigation on the effect of the nanopattern morphology on human bone marrow mesenchymal stem cells (BMMSC) and osteosarcoma cell line (SaOS-2). We applied principal component analysis (PCA) to quantify approximately 2000 cells per experimental condition using morphometric descriptors such as area, perimeter, aspect ratio, circularity, surface/area, and fractal dimension of cellular contour.[34a] In this study we used only PS-*b*-P2VP (i.e., same chemistry) with different size of the blocks and SVA to assemble nanopatterns. The PCA showed distinct response of BMMSC and SaOS-2 to the surface topography and chemistry. When PS-*b*-P2VP with low molecular weight was used to obtain the patterns, we observed similar results for BMMSC and SaOS-2 but the micellar nanopatterns assembled from high molecular weight BCP promote the spreading of BMMSC and have an opposite effect on SaOS-2, indicating that this topography is beneficial for bone regeneration after injury or pathology, e.g. bone fracture or tumor removal.

Lee *et al* delved into the effects of BCP nanopatterns on cell differentiation.[70] They used PS-*b*-PEG to create cylindrical nanopatterns through SVA in dodecylbenzenesulfonic acid, which is a good solvent for PEG. This method allows precise control over the pattern size: the diameter of the cylinders is tuned by the molecular weight of the BCP, while the height is modulated by the thickness of the deposited BCP/DBSA layer (Figure 14A). The results unveiled a correlation between MC3T3-E1 cell behavior and the size of the PS domains. Specifically, greater osteogenic differentiation was observed on larger PS domains (65±5 vs 85±5 nm).[70b] The authors proposed that cells with larger adhesion domains may induce cell differentiation by nucleus elongation. The focal adhesions and the generated mechanical forces can also promote changes in the nuclear shape, which in stem cells might trigger differentiation process.[71] These changes on the nucleus are also related the expression and disposition of lamin A/C. Stretched lamin A/C fibers promote nuclear stretching and are related to osteogenesis.[72] The differentiation process can be also influenced by the cylinders height: a

comparison between patterns with fixed diameter of the PS domains (57 nm) and different height (11, 23 and 43 nm, Figure 14B) showed that the intermediate height promotes the proliferation, cell spreading, and osteogenic differentiation (Figure 14C-E). This empirical evidence was not related with any mechanistic studies that can explain the preferred height of 23 nm.

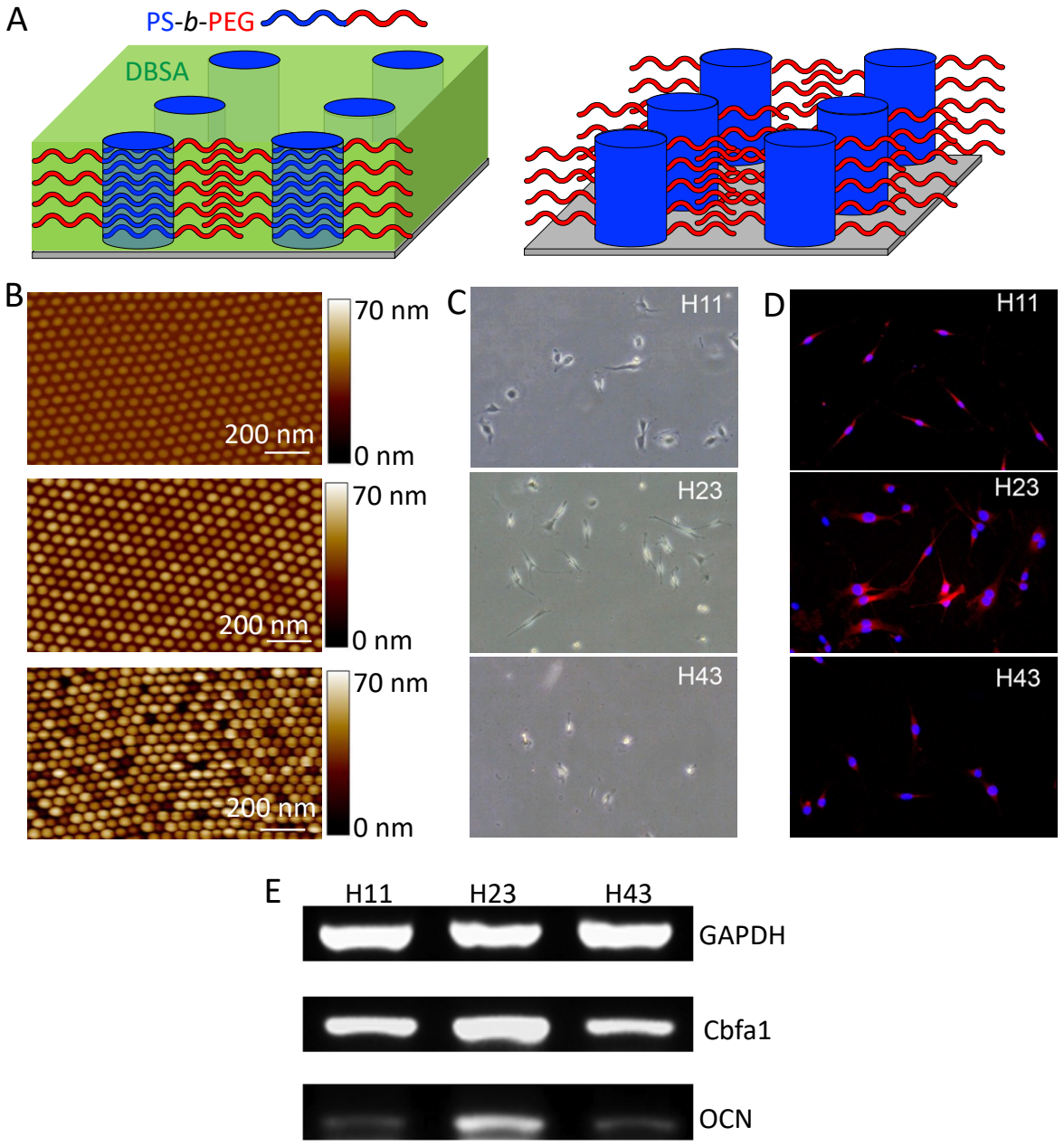

Figure 14. (A) Schematic presentation of the formation of cylindrical nanopatterns from PS-*b*-PEG by solvent annealing in dodecylbenzenesulfonic acid (DBSA). (B) AFM images

showing the generated patterns with different cylinders height. (C) Optical and (D) confocal scanning microscopy images of MC3T3-E1 in contact with cylindrical nanopatterns with height of 11, 23 and 43 nm. (E) Gene expression of osteogenic markers core-binding factor 1 (Cbfa1) and osteocalcin (OCN) after 14 days of MC3T3-E1 culture on the patterns. Glyceraldehyde 3-phosphate dehydrogenase (GAPDH) was used as a housekeeping gene. Adapted with permission.[70a] Copyright 2014, Elsevier.

In a similar approach, Shen *et al* used PS-*b*-PHEMA instead of PS-*b*-PEG.[58] HEMA is hydrophilic (although less than PEG) and as PEG prevents protein adsorption. Vertical cylinders of PS in a PHEMA matrix (PS diameter ~20 nm), parallel cylinders (width 15 nm) and vertical cylinders of PHEMA in a PS matrix (PHEMA diameter ~15 nm) were developed and studied with human prostate carcinoma cells DU145 and murine fibroblast cells NIH-3T3. The results showed that small PS domains (vertical PS cylinders) are cell repellent regardless the used cell line, while the other two patterns are comparable to homogeneous PHEMA. The mechanism of the cell repellence is unclear but may be related with limited proteins adsorption due to the small size of the PS domains.

Cooper-White *et al* provided experimental evidences supporting this potential cause. They investigated patterns assembled from PS-*b*-PEG copolymers with different molecular weights (PS_{50}-*b*-PEG_{11}, PS_{102}-*b*-PEG_{34}, and PS_{190}-*b*-PEG_{48}, molecular weight of each block is presented in kDa as subscript) and compared them to plain PS and tissue culture PS. When the PEG coverage was high (50% for PS_{50}-*b*-PEG_{11} and 59% for PS_{102}-*b*-PEG_{34}) a significant reduction in the protein adsorption (BSA, lysozyme and Fg) and cell adhesion (NIH-3T3 fibroblast) was observed.[64b] An opposite result was obtained for PS_{190}-*b*-PEG_{48}: the generated nanopattern has PEG coverage of 15% and high protein adsorption and cells adhesion was observed in this case. The protein coverage is not the only factor that influences the cell

adhesion. The morphology and the size of the protein pattern is also important as shown by Liu *et al* who investigated nanopatterns with different morphology assembled from PS_{45}-*b*-PI_{46} (cylindrical nanopattern) and PS_{65}-*b*-PI_{26} (lamellar nanopattern). They observed that fibronectin adsorbs on PS domains, i.e., copycat the BCP pattern, and influences the cell adhesion (CHO cell line). Higher cell density was observed on the cylindrical nanopatterns because of the higher local density of adhesive fibronectin ligands that enhance the integrin clustering thus strengthening focal adhesions.[59] Finally, the protein conformation on the patterns can also changes and thus, it is important to confirm the preserved bioactivity upon adsorption.[68]

An alternative approach involves covalent immobilization of the protein/peptide on the pattern (Figure 15). Cooper-White *et al* have developed different strategies for protein conjugation to the PEG block in PS-*b*-PEG and the bioactivity of the conjugated peptides/proteins was confirmed by cell culture on the patterned substrates. One strategy involves the modification of the hydroxyl terminal group of PEG with a maleimide. This end-on modification of PEG does not affect the micro-phase separation: the obtained PS-*b*-PEG-maleimide is spin coated and assembles in vertical PEG cylinders embedded in a PS matrix.[65a, 65b] In the following step, the PEGmaleimide domains can be functionalized with cysteine terminated peptides. The feasibility of this approach was demonstrated by functionalization with RGD motif - well known to promote cell adhesion. Indeed, an increased cell density (NIH-3T3 fibroblasts) was observed on the modified patterns.[65a] The addition of PS to the PS-*b*-PEG-maleimide can be used to tune the spacing between the RGD domains and to assess the effect of this spacing. Interestingly, patterns with spacing of 34 nm induced osteogenic differentiation of hMSC while spacing of 62 nm induced adipogenic phenotype.[65b] Besides RGD, other bioactive peptides (RRETAWA, IKVAV and YIGSR) have been conjugated to PS-*b*-PEG-maleimide alone or combined with RGD to induce different cell behavior: IKVAV induces osteogenesis,

RETTAWA and IKVAV - adipogenesis, and RGD is necessary to maintain mesenchymal stem cells for long culture times.[65c]

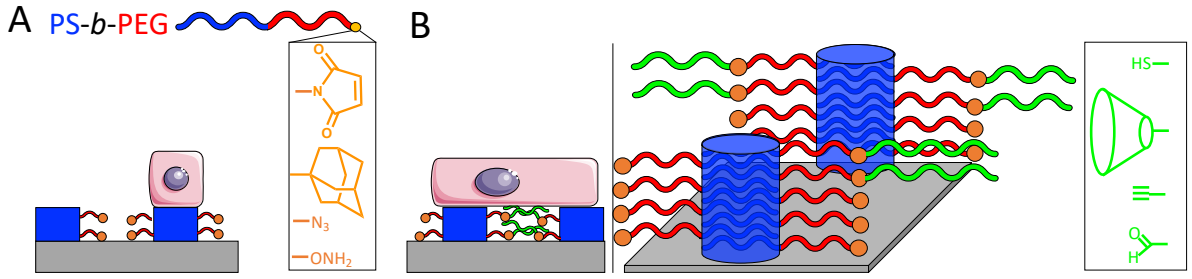

Figure 15. Schematic presentation of the platforms developed by Cooper-White *et al:* (A) PEG block is modified with maleimide, adamantine, azido or oxime functionality and the modified PS-b-PEG is self-assembled on a substrate; (B) The nanopattern is then biofunctionalized with peptide or protein that carries the complementary thiol, cyclodextrin, alkyne, or aldehyde group.

In a different strategy, PEG was functionalized with adamantine (Ada) and PS-*b*-PEG-Ada formed complex with peptides bearing the complementary β-cyclodextrin (β-CD) (Figure 15).[66a] This approach is not limited to peptides with cysteine terminal group because β-CD-NH2 is linked to the carboxyl at the C terminus, i.e. any peptide can be used. Click chemistry can be also employed in this context. PS-*b*-PEG-N_3 can be linked to alkyl terminated peptides using copper catalyzed protocol or an aldehyde terminated peptide can be conjugated to a PS-*b*-PEG-ONH_2 by oxime click chemistry.[67]

In illustrative examples, the Ada-β-CD [66a] and Huisgen click-oxime [67] methods were used to combine IKAV and RGD peptides and evaluate their biological effect on hMSC. The results showed that this combination of peptides modulate cells morphology and cytoskeletal actin organization, leading to an increased focal adhesion stability and maturation. To further advance the technology and promote hMSC differentiation into chondrocytes, a combinatorial

approach (array of 64 different combinations of 6 peptides) was developed.[66b] In this case, the Ada methodology was employed for conjugation with peptide sequences derived from ECM proteins (collagen I and II), transmembrane proteins (N-cadherin and E-cadherin), proteoglycan binding protein (decorin), and a glycosaminoglycan (heparin). These peptide sequences represent crucial components of cell-cell and cell-matrix interactions in osteogenic and chondrogenic environments. The composition was optimized towards chondrogenic or osteogenic differentiation that was confirmed by the collagen and GAG deposition as well as by gene expression. These works developed by Copper-White *et al* represent the forefront of the field, providing an advanced approach for fine-tuning cell adhesion and differentiation, specifically in the context of osteogenic, adipogenic, and chondrogenic differentiation.

The functionalization of the nanodomains with bioactives can be extended beyond proteins and peptides. Recently, we have demonstrated that PS-*b*-P2VP nanopatterns can be functionalized with heparin.[34b] The P2VP domains were quaternized with a diiodine linker to generate a charged surface that allowed to deposit heparin by electrostatic interactions. The heparnized BCP nanopatterns are antithrombotic and allowed reendothelialization (HUVEC cells).[34b]

4.3. Antibacterial BCP nanopatterns

Natural nanopatterned surfaces with antibacterial properties such as shark skin and cicada wings have inspired the development of bactericidal coatings that improve the contact between the implant and the soft tissue and reduce the risk of infection.[73] There are two mechanisms of action of such coatings: (i) the nanofeatures disrupt the membrane by mechanical forces (bactericidal effect); and (ii) the surface repeals the attachment of the bacteria (antiadhesive effect).[7c]

In our recent work, we have successfully developed bactericidal surfaces using PS-*b*-P2VP.[7a] This BCP was spin coated and subjected to SVA in toluene or chloroform to generate nanopatterns with distinct morphologies: micellar structures (Figure 16A), perforated lamellae (Figure 16B), and parallel cylinders (Figure 16C).

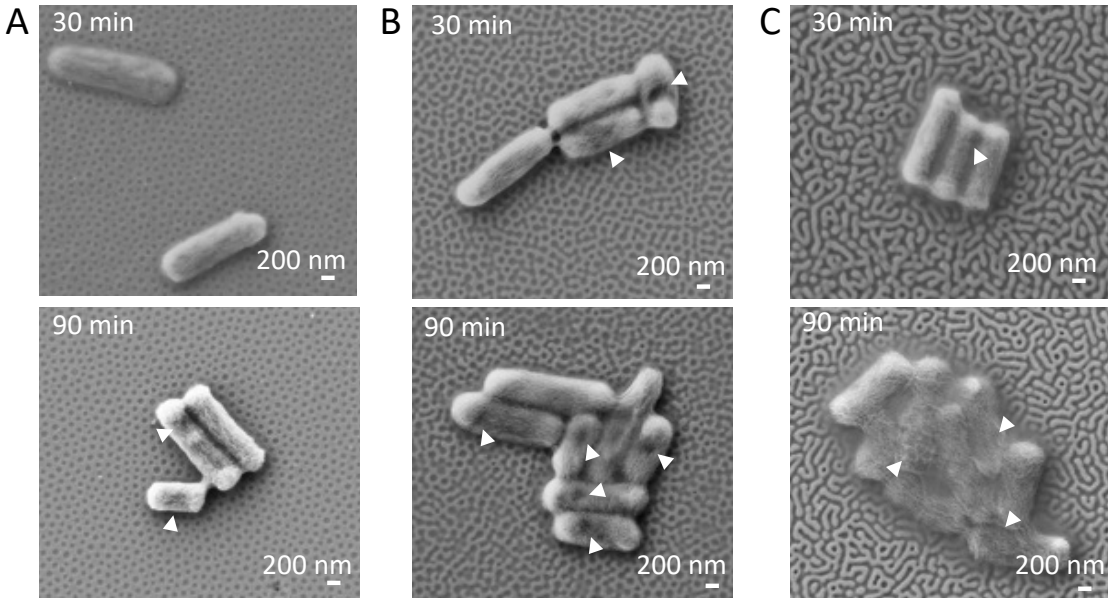

Figure 16. SEM micrographs on *E. coli* in contact with PS-b-P2VP nanopatterns: (A) micellar, (B) perforated lamellae and (C) parallel cylinders. Bacterial wall damage is pointed with white arrows. Adapted with permission.[7a] Copyright 2014, Elsevier.

Our results showed that the patterns had no effect on *S. aureus* bacteria, whereas the viability of *E. coli* bacteria was significantly reduced. This bactericidal effect was particularly pronounced for the cylindrical morphology (Figure 16C), resulting in 80-90% bacterial death. The mechanism behind this bactericidal effect involves the stretching of the bacterial cell wall upon adhesion to the nanopatterns, ultimately leading to wall rupture.[58] This mechanism is valid for the gram-negative bacteria, which have a less rigid wall and are more susceptible to mechanical stress. We observed this effect consistently across different substrates, including

glass and titanium commonly used for bone and dental implants.[7b] Of note, mammalian cells such as L929 cell line and gingival fibroblast cultured on top of the nanopatterns exhibited good adhesion and remained viable.

Similar approach was also reported by Shuyan Li *et al*.[74] They used microphase separation of PS-*b*-PMMA to generate vertical and parallel cylinders, and investigated their interaction with *E. coli* and *S. aureus* by AFM. *S. Aureus* adhered to both nanopatterns, while *E. coli* was only found on the parallel cylinders but not on the vertical cylinders, suggesting an antifouling effect of the latter. These results are different from our own observation with PS-*b*-P2VP nanopatterns (bacteria adhered to all nanopatterns) and highlight the importance of surface chemistry in conjunction with nanomorphology: in the case of PS-*b*-PMMA, both blocks are hydrophobic.

Moore *et al* used BCP nanopatterns as substrates to adhere antibacterial molecules.[75] They studied the virucidal and bactericidal effect of PS-*b*-P4VP functionalized with C_{70} (fullerene, known because of its virucidal effect) at the PS domains and silver nanoparticles (antibacterial) at the P4VP domains. The pattern with silver nanoparticles had a strong antibacterial capacity, while a moderate antibacterial effect was observed for the BCP nanopatterns *per se*.

Besides these few examples, the application of BCP nanopatterns as antibacterial and bactericidal substrates is just emerging and future research should focus on the design and use of BCP with bioactive blocks. Biopolymers synthetized and secreted by different organisms represent a large and diverse molecular set that can be searched for such blocks using computational and simulation tools. Of note, biopolymers have an additional advantage - most of them are generally regarded as safe by FDA.

5. Conclusions and outlook

The application of BCP nanopatterns have been successfully extended from the electronics to the biomaterials field because of the possibility to coat large surface areas with nanofeatures and to create different morphologies with control over the domain sizes. While the current state of the art of BCP nanopatterns for bioapplications emphases their use as arrays for immobilization or deposition of bioactive molecules, the field is still in its infancy considering the limited number of studied BCP and morphologies: mostly BCP of the hydrophobic PS block and the hydrophilic PEG, PMMA, and, in a few examples, HEMA blocks have been reported. Keeping in mind the unlimited diversity of morphologies that can be developed by microphase separation, very few (and simple) nanostructures. Complex triblock copolymer patterns and the possibility to pattern different proteins on the same substrates are underexplored. Immobilization of other bioactive molecules beyond peptides and proteins (e.g. glycans and DNA) are also unexploited. The breakthroughs in the field will likely come from the exploration of these possibilities as they allow development of complex structures with precise control that have enormous biological potential.

Acknowledgements:

We acknowledge the support from the Portuguese Foundation for Science and Technology (grants PTDC/QUI-POL/28117/2017, PD/BD/128085/2016, and CEECIND/00814/2017) and the European fund for regional development via the Operational Programme for Competitiveness and Internalization (grant POCI-01-0145-FEDER-028117).

References:

[1] a)J. J. Luo, M. Walker, Y. B. Xiao, H. Donnelly, M. J. Dalby, M. Salmeron-Sanchez, *Bioact Mater* **2022**, 15, 145; b)L. C. Y. Lee, N. Gadegaard, M. C. de Andres, L. A. Turner, K.

V. Burgess, S. J. Yarwood, J. Wells, M. Salmeron-Sanchez, D. Meek, R. O. C. Oreffo, M. J. Dalby, *Biomaterials* **2017**, 116, 10; c)C. Franke, T. Chum, Z. Kvicalova, D. Glatzova, G. J. Gentsch, A. Rodriguez, D. A. Helmerich, L. Herdly, H. Mavila, O. Frank, T. Brdicka, S. van de Linde, M. Cebecauer, *Commun Biol* **2022**, 5, 218.

[2] a)R. K. Silverwood, P. G. Fairhurst, T. Sjostrom, F. Welsh, Y. X. Sun, G. Li, B. Yu, P. S. Young, B. Su, R. M. D. Meek, M. J. Dalby, P. M. Tsimbouri, *Advanced Healthcare Materials* **2016**, 5, 947; b)K. Li, S. W. Liu, T. Hu, I. Razanau, X. D. Wu, H. Y. Ao, L. P. Huang, Y. T. Xie, X. B. Zheng, *Acs Biomater Sci Eng* **2020**, 6, 969; c)X. Y. Sun, M. K. Driscoll, C. Guven, S. Das, C. A. Parent, J. T. Fourkas, W. Losert, *P Natl Acad Sci USA* **2015**, 112, 12557; d)S. Cao, Q. Yuan, *Biomat Transl* **2022**, 3, 55; e)A. Bachhuka, B. Delalat, S. R. Ghaemi, S. Gronthos, N. H. Voelcker, K. Vasilev, *Nanoscale* **2017**, 9, 14248; f)A. V. Singh, M. Ferri, M. Tamplenizza, F. Borghi, G. Divitini, C. Ducati, C. Lenardi, C. Piazzoni, M. Merlini, A. Podesta, P. Milani, *Nanotechnology* **2012**, 23, 475101; g)A. M. Loye, E. R. Kinser, S. Bensouda, M. Shayan, R. Davis, R. Wang, Z. Chen, U. D. Schwarz, J. Schroers, T. R. Kyriakides, *Sci Rep-Uk* **2018**, 8, 8758.

[3] Y. S. Yun, E. H. Kang, S. Ji, S. B. Lee, Y. O. Kim, I. S. Yun, J. S. Yeo, *Adv Biosyst* **2020**, 4, 2000092.

[4] C. M. Bates, M. J. Maher, D. W. Janes, C. J. Ellison, C. G. Willson, *Macromolecules* **2014**, 47, 2.

[5] a)M. L. Wu, D. Wang, L. J. Wan, *Nat Commun* **2016**, 7, 10752; b)J. A. Chai, F. W. Huo, Z. J. Zheng, L. R. Giam, W. Shim, C. A. Mirkin, *P Natl Acad Sci USA* **2010**, 107, 20202; c)M. Arnold, V. C. Hirschfeld-Warneken, T. Lohmuller, P. Heil, J. Blummel, E. A. Cavalcanti-Adam, M. Lopez-Garcia, P. Walther, H. Kessler, B. Geiger, J. P. Spatz, *Nano Letters* **2008**, 8, 2063.

[6] A. Rosler, G. W. M. Vandermeulen, H. A. Klok, *Advanced Drug Delivery Reviews* **2012**, 64, 270.

[7] a)R. Fontelo, D. S. da Costa, R. L. Reis, R. Novoa-Carballal, I. Pashkuleva, *Acta Biomaterialia* **2020**, 112, 174; b)R. Fontelo, D. Soares da Costa, M. Gomez-Florit, H. Tiainen, R. L. Reis, R. Novoa-Carballal, I. Pashkuleva, *Journal of Materials Chemistry B* **2022**, 10, 8710; c)K. Modaresifar, S. Azizian, M. Ganjian, L. E. Fratila-Apachitei, A. A. Zadpoor, *Acta Biomaterialia* **2019**, 83, 29.

[8] a)C. Jin, B. C. Olsen, E. J. Luber, J. M. Buriak, *Chemistry of Materials* **2017**, 29, 176; b)Y. Y. Mai, A. Eisenberg, *Chem Soc Rev* **2012**, 41, 5969.

[9] a)M. W. Matsen, F. S. Bates, *Macromolecules* **1996**, 29, 1091; b)M. W. Matsen, M. Schick, *Physical Review Letters* **1994**, 72, 2660; c)F. S. Bates, G. H. Fredrickson, *Physics Today* **1999**, 52, 32.

[10] Y. C. Tseng, S. B. Darling, *Polymers-Basel* **2010**, 2, 470.

[11] J. E. Poelma, K. Ono, D. Miyajima, T. Aida, K. Satoh, C. J. Hawker, *Acs Nano* **2012**, 6, 10845.

[12] A. D. Goodson, J. E. Troxler, M. S. Rick, H. S. Ashbaugh, J. N. L. Albert, *Macromolecules* **2019**, 52, 9389.

[13] a)X. D. Gu, I. Gunkel, T. P. Russell, *Philos T R Soc A* **2013**, 371, 20120306; b)G. O. R. A. van Ekenstein, R. Meyboom, G. ten Brinke, O. Ikkala, *Macromolecules* **2000**, 33, 3752.

[14] W. H. Li, M. J. Liu, F. Qiu, A. C. Shi, *J Phys Chem B* **2013**, 117, 5280.

[15] M. J. Liu, W. H. Li, F. Qiu, A. C. Shi, *Macromolecules* **2012**, 45, 9522.

[16] U. Breiner, U. Krappe, R. Stadler, *Macromol Rapid Comm* **1996**, 17, 567.

[17] H. K. Choi, A. Nunns, X. Y. Sun, I. Manners, C. A. Ross, *Advanced Materials* **2014**, 26, 2474.

[18] S. X. Ji, L. Wan, C. C. Liu, P. F. Nealey, *Prog Polym Sci* **2016**, 54-55, 76.

[19] A. Knoll, A. Horvat, K. S. Lyakhova, G. Krausch, G. J. A. Sevink, A. V. Zvelindovsky, R. Magerle, *Physical Review Letters* **2002**, 89, 035501.

[20] H. Ogawa, M. Takenaka, T. Miyazaki, A. Fujiwara, B. Lee, K. Shimokita, E. Nishibori, M. Takata, *Macromolecules* **2016**, 49, 3471.

[21] a)A. Boker, A. H. E. Muller, G. Krausch, *Macromolecules* **2001**, 34, 7477; b)S. Roland, R. E. Prud'homme, C. G. Bazuin, *Acs Macro Letters* **2012**, 1, 973.

[22] P. W. Majewski, K. G. Yager, *Nano Letters* **2015**, 15, 5221.

[23] S. R. Nowak, K. G. Yager, *Adv Mater Interfaces* **2020**, 7, 1901679.

[24] a)M. Ruppel, C. W. Pester, K. M. Langner, G. J. A. Sevink, H. G. Schoberth, K. Schmidt, V. S. Urban, J. W. Mays, A. Boker, *Acs Nano* **2013**, 7, 3854; b)S. Sakurai, *Polymer* **2008**, 49, 2781.

[25] a)A. Modi, S. M. Bhaway, B. D. Vogt, J. F. Douglas, A. Al-Enizi, A. Elzatahry, A. Sharma, A. Karim, *Acs Appl Mater Inter* **2015**, 7, 21639; b)W. I. Park, J. M. Kim, J. W. Jeong, Y. S. Jung, *Acs Nano* **2014**, 8, 10009.

[26] K. W. Gotrik, C. A. Ross, *Nano Letters* **2013**, 13, 5117.

[27] a)X. J. Zhang, K. D. Harris, N. L. Y. Wu, J. N. Murphy, J. M. Buriak, *Acs Nano* **2010**, 4, 7021; b)C. Jin, J. N. Murphy, K. D. Harris, J. M. Buriak, *Acs Nano* **2014**, 8, 3979.

[28] P. W. Majewski, K. G. Yager, *Acs Nano* **2015**, 9, 3896.

[29] F. Ferrarese Lupi, T. J. Giammaria, G. Seguini, F. Vita, O. Francescangeli, K. Sparnacci, D. Antonioli, V. Gianotti, M. Laus, M. Perego, *Acs Appl Mater Inter* **2014**, 6, 7180.

[30] a)J. D. Cushen, I. Otsuka, C. M. Bates, S. Halila, S. Fort, C. Rochas, J. A. Easley, E. L. Rausch, A. Thio, R. Borsali, C. G. Willson, C. J. Ellison, *Acs Nano* **2012**, 6, 3424; b)L. M. Pitet, S. F. Wuister, E. Peeters, E. J. Kramer, C. J. Hawker, E. W. Meijer, *Macromolecules* **2013**, 46, 8289.

[31] a)X. D. Gu, I. Gunkel, A. Hexemer, T. P. Russell, *Macromolecules* **2016**, 49, 3373; b)K. W. Gotrik, A. F. Hannon, J. G. Son, B. Keller, A. Alexander-Katz, C. A. Ross, *Acs Nano* **2012**, 6, 8052; c)E. Han, K. O. Stuen, Y. H. La, P. F. Nealey, P. Gopalan, *Macromolecules* **2008**, 41, 9090; d)S. S. Dinachali, W. B. Bai, K. H. Tu, H. K. Choi, J. S. Zhang, M. E. Kreider, L. C. Cheng, C. A. Ross, *Acs Macro Letters* **2015**, 4, 500; e)R. Lundy, S. P. Flynn, C. Cummins, S. M. Kelleher, M. N. Collins, E. Dalton, S. Daniels, M. A. Morris, R. Enright, *Physical Chemistry Chemical Physics* **2017**, 19, 2805.

[32] a)J. N. L. Albert, T. H. Epps, *Materials Today* **2010**, 13, 24; b)J. Peng, Y. Xuan, H. F. Wang, Y. M. Yang, B. Y. Li, Y. C. Han, *Journal of Chemical Physics* **2004**, 120, 11163.

[33] a)Y. S. Jung, C. A. Ross, *Advanced Materials* **2009**, 21, 2540; b)H. Y. Huang, F. J. Zhang, Z. J. Hu, B. Y. Du, T. B. He, F. K. Lee, Y. J. Wang, O. K. C. Tsui, *Macromolecules* **2003**, 36, 4084; c)M. Vayer, M. A. Hillmyer, M. Dirany, G. Thevenin, R. Erre, C. Sinturel, *Thin Solid Films* **2010**, 518, 3710; d)S. H. Kim, M. J. Misner, T. Xu, M. Kimura, T. P. Russell, *Advanced Materials* **2004**, 16, 226.

[34] a)R. Fontelo, D. S. da Costa, R. L. Reis, R. Novoa-Carballal, I. Pashkuleva, *Colloids and Surfaces B: Biointerfaces* **2022**, 219, 112774; b)R. Fontelo, D. Soares da Costa, R. L. Reis, R. Novoa-Carballal, I. Pashkuleva, *Journal of Colloid and Interface Science* **2022**, 608, 1608.

[35] C. Sinturel, M. Vayer, M. Morris, M. A. Hillmyer, *Macromolecules* **2013**, 46, 5399.

[36] a)E. Han, H. M. Kang, C. C. Liu, P. F. Nealey, P. Gopalan, *Advanced Materials* **2010**, 22, 4325; b)S. J. Jeong, J. E. Kim, H. S. Moon, B. H. Kim, S. M. Kim, J. B. Kim, S. O. Kim, *Nano Letters* **2009**, 9, 2300.

[37] a)D. Sundrani, S. B. Darling, S. J. Sibener, *Nano Letters* **2004**, 4, 273; b)K. Brassat, D. Kool, C. G. A. Nallet, J. K. N. Lindner, *Adv Mater Interfaces* **2020**, 7.

[38] J. Chai, J. M. Buriak, *Acs Nano* **2008**, 2, 489.

[39] D. H. Kim, H. G. Kwon, H. K. Choi, *Polymers-Basel* **2023**, 15.

[40] S. Kim, W. J. Kang, C. H. Jung, M. Kim, K. W. Kim, M. Go, N. Jeon, J. Rho, J. U. Kim, J. K. Kim, *Macromolecules* **2023**, 56, 1837.

[41] L. Q. Wang, Z. M. Tang, D. Li, J. P. Lin, Z. Guan, *Nanoscale* **2020**, 12, 13119.

[42] Y. Han, C. H. Cai, J. P. Lin, S. T. Gong, W. H. Xu, R. Hu, *Macromol Rapid Comm* **2018**, 39.

[43] W. H. Xu, Z. W. Xu, C. H. Cai, J. P. Lin, S. M. Zhang, L. S. Zhang, S. L. Lin, Y. Yao, H. M. Qi, *J Phys Chem Lett* **2019**, 10, 6375.

[44] a)Z. M. Tang, D. Li, J. P. Lin, L. S. Zhang, C. H. Cai, Y. Yao, C. M. Yang, X. H. Tian, *Polym Chem-Uk* **2020**, 11, 7487; b)B. Sun, Z. W. Xu, Z. M. Tang, C. H. Cai, J. P. Lin, *Macromol Chem Phys* **2020**, 221; c)Z. M. Tang, Z. W. Xu, C. H. Cai, J. P. Lin, Y. Yao, C. M. Yang, X. H. Tian, *Macromol Rapid Comm* **2020**, 41.

[45] J. S. Silverstein, B. J. Casey, P. Kofinas, B. J. Dair, *Journal of Nanoscience and Nanotechnology* **2016**, 16, 1460.

[46] J. Malmstrom, A. Wason, F. Roache, N. A. Yewdall, M. Radjainia, S. H. Wei, M. J. Higgins, D. E. Williams, J. A. Gerrard, J. Travas-Sejdic, *Nanoscale* **2015**, 7, 19940.

[47] T. Kollmetz, I. Monteiro, J. A. Gerrard, J. Malmstrom, *Acs Omega* **2020**, 5, 26365.

[48] S. Song, M. Milchak, H. B. Zhou, T. Lee, M. Hanscom, J. I. Hahm, *Nanotechnology* **2013**, 24, 095601.

[49] N. Kumar, O. Parajuli, J. I. Hahm, *J Phys Chem B* **2007**, 111, 4581.

[50] a)N. Kumar, O. Parajuli, A. Dorfman, D. Kipp, J. I. Hahm, *Langmuir* **2007**, 23, 7416; b)N. Kumar, O. Parajuli, A. Gupta, J. I. Hahm, *Langmuir* **2008**, 24, 2688; c)O. Parajuli, A. Gupta, N. Kumar, J. I. Hahm, *J Phys Chem B* **2007**, 111, 14022.

[51] N. Kumar, J. I. Hahm, *Langmuir* **2005**, 21, 6652.

[52] a)S. Song, K. Ravensbergen, A. Alabanza, D. Soldin, J. I. Hahm, *Acs Nano* **2014**, 8, 5257; b)T. Xie, J. Chattoraj, P. J. Mulcahey, N. P. Kelleher, E. Del Gado, J. I. Hahm, *Nanoscale* **2018**, 10, 9063; c)S. Song, T. Xie, K. Ravensbergen, J. I. Hahm, *Nanoscale* **2016**, 8, 3496.

[53] K. H. A. Lau, J. Bang, D. H. Kim, W. Knoll, *Advanced Functional Materials* **2008**, 18, 3148.

[54] D. Liu, T. Wang, J. L. Keddie, *Langmuir* **2009**, 25, 4526.

[55] L. Shen, J. T. Zhu, *Macromol Rapid Comm* **2016**, 37, 494.

[56] L. Shen, A. Garland, Y. N. Wang, Z. C. Li, C. W. Bielawski, A. Guo, X. Y. Zhu, *Small* **2012**, 8, 3169.

[57] D. H. Cho, J.-i. Hahm, *The Journal of Physical Chemistry B* **2021**, 125, 6040.

[58] L. Shen, J. Xie, J. Tao, J. Zhu, *Journal of Materials Chemistry B* **2015**, 3, 1157.

[59] D. Liu, C. A. C. Abdullah, R. P. Sear, J. L. Keddie, *Soft Matter* **2010**, 6, 5408.

[60] H. Tran, K. Ronaldson, N. A. Bailey, N. A. Lynd, K. L. Killops, G. Vunjak-Novakovic, L. M. Campos, *Acs Nano* **2014**, 8, 11846.

[61] M. Arnold, E. A. Cavalcanti-Adam, R. Glass, J. Blummel, W. Eck, M. Kantlehner, H. Kessler, J. P. Spatz, *Chemphyschem* **2004**, 5, 383.

[62] a)E. A. Cavalcanti-Adam, A. Micoulet, J. Blummel, J. Auernheimer, H. Kessler, J. P. Spatz, *European Journal of Cell Biology* **2006**, 85, 219; b)R. Glass, M. Moller, J. P. Spatz, *Nanotechnology* **2003**, 14, 1153; c)C. Selhuber-Unkel, M. López-García, H. Kessler, J. P. Spatz, *Biophysical Journal* **2008**, 95, 5424.

[63] S. Jaehrling, K. Thelen, T. Wolfram, G. E. Pollerberg, *Nano Letters* **2009**, 9, 4115.

[64] a)I. A. Monteiro, T. Kollmetz, D. S. Musson, S. R. McGlashan, J. Malmstrom, *Biointerphases* **2020**, 15, 011003; b)P. A. George, B. C. Donose, J. J. Cooper-White, *Biomaterials* **2009**, 30, 2449.

[65] a)P. A. George, M. R. Doran, T. I. Croll, T. P. Munro, J. J. Cooper-White, *Biomaterials* **2009**, 30, 4732; b)J. E. Frith, R. J. Mills, J. J. Cooper-White, *Journal of Cell Science* **2012**, 125, 317; c)J. E. Frith, R. J. Mills, J. E. Hudson, J. J. Cooper-White, *Stem Cells and Development* **2012**, 21, 2442.

[66] a)H. Q. Li, J. Frith, J. J. Cooper-White, *Biomacromolecules* **2014**, 15, 43; b)S. Camarero-Espinosa, J. J. Cooper-White, *Biomaterials* **2019**, 210, 105.

[67] H. Li, J. J. Cooper-White, *Biomaterials Science* **2014**, 2, 1693.

[68] T. Xie, A. Vora, P. J. Mulcahey, S. E. Nanescu, M. Singh, D. S. Choi, J. K. Huang, C. C. Liu, D. P. Sanders, J. I. Hahm, *Acs Nano* **2016**, 10, 7705.

[69] H. L. Khor, Y. Kuan, H. Kukula, K. Tamada, W. Knoll, M. Moeller, D. W. Hutmacher, *Biomacromolecules* **2007**, 8, 1530.

[70] a)E. J. Jeong, J. W. Lee, Y. J. Kwark, S. H. Kim, K. Y. Lee, *Colloids and Surfaces B-Biointerfaces* **2014**, 123, 679; b)S. J. Yeon, J. W. Lee, J. W. Lee, E. J. Jeong, Y. J. Kwark, S. H. Kim, K. Y. Lee, *Soft Matter* **2012**, 8, 3898.

[71] I. Casanellas, A. Lagunas, Y. Vida, E. Perez-Inestrosa, J. A. Andrades, J. Becerra, J. Samitier, *Biomimetics-Basel* **2019**, 4, 43.

[72] Y. Hou, W. Y. Xie, L. X. Yu, L. C. Camacho, C. X. Nie, M. Zhang, R. Haag, Q. Wei, *Small* **2020**, 16, 1905422.

[73] P. Ramburrun, N. A. Pringle, A. Dube, R. Z. Adam, S. D'Souza, M. Aucamp, *Materials* **2021**, 14, 3167.

[74] S. Y. Li, A. Komaromy, R. I. Boysen, D. V. Nicolau, M. T. W. Hearn, *Biomedical Applications of Micro- and Nanoengineering Iv and Complex Systems* **2008**, 7270, 727008.

[75] K. J. Moor, C. O. Osuji, J. H. Kim, *Acs Appl Mater Inter* **2016**, 8, 33583.